

# The scale and redshift variation of density and velocity distributions in dark matter flow and two-thirds law for pairwise velocity

Zhijie (Jay) Xu,<sup>1\*</sup>

<sup>1</sup>Physical and Computational Sciences Directorate, Pacific Northwest National Laboratory; Richland, WA 99352, USA

Accepted XXX. Received YYY; in original form ZZZ

## ABSTRACT

A halo-based non-projection approach is proposed to study the scale and redshift dependence of density and velocity distributions (PDF) in dark matter flow. All particles are divided into halo and out-of-halo particles such that PDF can be studied separately. Without projecting particle fields onto grid, scale dependence is analyzed by counting all pairs on different scales  $r$ . Redshift dependence is studied via generalized kurtosis. From this analysis, we can demonstrate: i) Delaunay tessellation can be used to reconstruct density field. Density correlations/spectrum are obtained, modeled and compared with theory; ii)  $m$ th moment of pairwise velocity can be analytically modelled. On small scale, even order moments can be modelled by a two-thirds law  $\langle(\Delta u_L)^{2n}\rangle \propto (-\epsilon_u r)^{2/3}$ , while odd order moments  $\langle(\Delta u_L)^{2n+1}\rangle = (2n+1)\langle(\Delta u_L)^{2n}\rangle\langle\Delta u_L\rangle \propto r$  and satisfy a generalized stable clustering hypothesis (GSCH); iii) Scale dependence is studied for longitudinal velocity  $u_L$  or  $u'_L$ , pairwise velocity (velocity difference)  $\Delta u_L = u'_L - u_L$  and velocity sum  $\Sigma u_L = u'_L + u_L$ . Fully developed velocity fields are never Gaussian on any scale; iv) On small scale, both  $u_L$  and  $\Sigma u_L$  can be modelled by a  $X$  distribution to maximize system entropy. Distributions of  $\Delta u_L$  is different with its moments analytically derived; v) On large scale, both  $\Delta u_L$  and  $\Sigma u_L$  can be modelled by a logistic function; vi) Redshift evolution of velocity distributions follows prediction of  $X$  distribution with a decreasing shape parameter  $\alpha(z)$  to continuously maximize system entropy.

**Key words:** Dark matter; N-body simulations; Theoretical models

## CONTENTS

- 1 Introduction
- 2 N-body simulations and numerical data
- 3 Density distribution, correlation, and spectrum functions
  - 3.1 One-point probability distributions of density field
  - 3.2 Two-point statistical measures of density field
  - 3.3 Statistical measures of density from N-body simulation
  - 3.4 Modeling second order statistical measures of density field
- 4 Characterizing probability distributions of velocity fields
  - 4.1 Generalized kurtosis, moments, and structure functions
  - 4.2 Generalized kurtosis of velocity from N-body simulation
  - 4.3 First moment of velocity and pair conservation equation
  - 4.4 Second moment of velocity field
  - 4.5 Two-thirds law for even order moments of pairwise velocity
  - 4.6 GSCH for odd order moments of pairwise velocity
- 5 Redshift and scale variation of velocity distributions
  - 5.1 Modeling velocity distributions on small scale
  - 5.2 Distribution of pairwise velocity on small scale
  - 5.3 Velocity distributions on intermediate scale
  - 5.4 Modeling velocity distributions on large scale
  - 5.5 Redshift evolution of velocity distributions
- 6 Conclusions

## 1 INTRODUCTION

The cosmic peculiar velocity and density fields contain rich information for the dynamics of self-gravitating collisionless dark matter flow (SG-CFD) from large scale to the highly non-linear small scales. Statistics of velocity and density fields is crucial for fundamental questions regarding structure formation and dynamics. The statistical analysis of velocity fields was previously applied to describe the evolution of a system of self-gravitating collisionless particles using BBGKY equations (Davis & Peebles 1977). The pairwise velocity has been introduced to probe the cosmological density parameter (Ferreira et al. 1999; Juszkiewicz et al. 2000), and the two-point correlation function was introduced to quantify the cosmic velocity field from real dataset (Gorski 1988; Gorski et al. 1989).

In addition, velocity distribution has profound implications for detection experiments. For predicted DM-nucleon scattering in direct detection (Kuhlen et al. 2010; Ullio & Kamionkowski 2001), the detection rate of scattering is proportional to the inverse (or -1) moment of distribution. That rate is very sensitive to the high velocity tail of distribution. For indirect search (Zhao et al. 2018; Petac et al. 2018), the annihilation cross section is directly dependent on the distribution of relative velocity. Velocity distribution of dark matter particles is expected to be different from Maxwell-Boltzmann. This is confirmed by simulations (Kazantzidis et al. 2004; Wojtak et al. 2008) and theory from maximum entropy principle (Xu 2021c,e).

The one-point distribution of matter density is another fundamental property for gravitational lensing and nonlinear clustering. The study of matter density has a long history dating back to 1930s when

\* E-mail: zhijie.xu@pnnl.gov; zhijie.xu@hotmail.com

Hubble found the matter distribution is non-Gaussian and can be approximate by log-normal distribution (Hubble 1934). The interests and efforts are still ongoing both theoretically and numerically (Bernardeau & Kofman 1995; Klypin et al. 2018).

While directly measuring velocity and density fields from real samples is still challenging in practice, tremendous information can be obtained from N-body simulation, an invaluable tool to study the dynamics of collisionless dark matter flow in both linear and nonlinear regime (Angulo et al. 2012; Springel 2005; Peebles et al. 1989; Efstathiou et al. 1985). However, it is not a trivial task to extract and characterize the statistics of velocity and density fields from N-body simulations. There is a fundamental problem as velocity and density are only sampled at discrete locations of particle position in N-body simulations. That sampling has a poor quality at locations with low particle density (Jennings et al. 2011).

The standard approach computes the power spectrum of velocity, density (and its gradients) in Fourier space (Hahn et al. 2015; Pueblas & Scoccimarro 2009; Jelic-Cizmek et al. 2018), where cloud-in-cell (CIC) (Hockney & Eastwood 1988) or triangular-shaped-cloud (TSC) schemes are used to project density and velocity fields onto regular structured grids. This will unavoidably introduce sampling errors in density and velocity fields (Baugh & Efstathiou 1994; Baugh et al. 1995). Both real-space and Fourier-space data contain the same information, while directly working in real-space data avoids the information distortion due to field projection and the associated errors due to the conversion between Fourier- and real-space.

In this paper, a new halo-based non-projection approach is proposed for statistical analysis of density and velocity fields:

- (i) Instead of projecting particle fields onto structured grid, analysis is performed in real space by the statistics over all particle pairs on different scales. This will maximumly preserve and utilize the information from N-body simulation;
- (ii) Based on the halo description of N-body system, distributions should evolve differently in halos and out-of-halo region. Therefore, all halos in N-body system are identified and all particles are divided into halo and out-of-halo particles such that relevant distributions can be studied separately;
- (iii) Scale and redshift dependence of distributions can be studied by the variation of generalized kurtosis for a given distribution.

From this practice, tremendous amount of knowledge was learned that can be compared with the statistical theory of isotropic, homogeneous, and incompressible turbulence (Taylor 1935, 1938; de Karman & Howarth 1938; Batchelor 1953). One example is the distribution of pairwise velocity. For incompressible flow, there exist an inertial range of scales in energy spectrum with a constant energy flux followed by a dissipation range dominant by viscous force. A universal form was established for  $m$ th order longitudinal velocity structure function ( $m$ th moment of pairwise velocity in cosmological terms) in inertial range (Kolmogorov 1962),

$$S_m^{lp}(r) = \left\langle \left( u'_L - u_L \right)^m \right\rangle = \beta_m (\varepsilon_u)^{m/3} r^{m/3}, \quad (1)$$

where  $u'_L$  and  $u_L$  are longitudinal velocities,  $\beta_m$  is a universal constant, and  $\varepsilon_u$  is the energy dissipation rate.

Specifically, the second order structure function (i.e. pairwise velocity dispersion)  $S_2^{lp}(r) = \beta_2 \varepsilon_u r^{2/3}$  with  $\beta_2 \approx 2$  is known as the two-thirds law, while  $S_2^{lp}(r) \propto r^2$  in the dissipation range where viscous force is dominant. The third order structure function  $S_3^{lp}(r) = -4/5 \varepsilon_u r$  with  $\beta_3 = -4/5$  is known as the four-fifths law that can be exactly derived from Navier-stokes equation (de Karman & Howarth 1938). Similarly,  $S_3^{lp}(r) \propto r^3$  in the dissipation range

**Table 1.** Numerical parameters of N-body simulation

Run	$\Omega_0$	$\Lambda$	$h$	$\Gamma$	$\sigma_8$	$L$ (Mpc/h)	$N$	$m_p$ $M_\odot/h$	$l_{soft}$ (Kpc/h)
SCDM1	1.0	0.0	0.5	0.5	0.51	239.5	$256^3$	$2.27 \times 10^{11}$	36

for incompressible flow. However, dark matter flow exhibits completely different behavior due to collisionless nature and long-range interaction, as we will demonstrate in this paper.

By studying the scale and redshift variation of density and velocity distributions in dark matter flow using the proposed halo-based non-projection approach, we can

- (i) obtain the redshift evolution of one-point density and log-density distributions for halo and out-of-halo particles along with analytical models for two-point density statistical measures;
- (ii) demonstrate that velocity fields are non-Gaussian on all scales despite that they can be initially Gaussian;
- (iii) model velocity distributions separately on small and large scales along with their redshift variation;
- (iv) identify a universal two-thirds law for (reduced) even order structure functions and liner scaling for all odd order structure functions (or generalized stable clustering hypothesis GSCH).

In addition to the density and velocity, there exist acceleration fluctuations in dark matter flow and distributions of acceleration due to the long-range gravitational interaction. The fluctuation of acceleration in halos ( $\sim 10^{-10} m/s^2$ ) matches the critical acceleration  $a_0$  in MOND, which can be further determined by the rate of energy cascade  $\varepsilon_u = -a_0 u / (3\pi)^2$  (Xu 2022j). Here  $u$  is the one-dimensional velocity dispersion of all particles in system (see Xu 2022e, Eq. (1)). In addition, the baryonic-to-halo mass ratio is also closely related to the energy cascade in dark matter flow (Xu 2022k).

Finally, this paper is organized as follows: Section 2 introduces the N-body simulation data, followed by statistical measures for density in Section 3. The redshift and scale dependence of velocity distributions are presented and modeled in Sections 4 and 5.

## 2 N-BODY SIMULATIONS AND NUMERICAL DATA

The numerical data were public available and generated from the N-body simulations carried out by the Virgo consortium. A comprehensive description of the data can be found in (Frenk et al. 2000; Jenkins et al. 1998). As the first step, the current study was carried out using the simulation runs with  $\Omega = 1$  and the standard CDM power spectrum (SCDM) to focus on the matter-dominant gravitational flow of collisionless matter. Similar analysis can be extended to other simulations with different model assumptions in the future. The same set of data has been widely used in studies from clustering statistics (Jenkins et al. 1998) to formation of cluster halos in large scale environment (Colberg et al. 1999), and test of models for halo abundances and mass functions (Sheth et al. 2001a). More details on simulation parameters are provided in Table 1.

Two relevant datasets from this N-body simulation, i.e. halo-based and correlation-based statistics of dark matter flow, can be found at Zenodo.org (Xu 2022a,b), along with the accompanying presentation slides, "A comparative study of dark matter flow & hydrodynamic turbulence and its applications" (Xu 2022c). All data files are also available on GitHub (Xu 2022d).

### 3 DENSITY DISTRIBUTION, CORRELATION, AND SPECTRUM FUNCTIONS

Various statistical measures can be introduced to characterize the velocity field in self-gravitating collisionless flow (Xu 2022e,f,h), i.e. the real-space correlation, dispersion and structure functions, and power spectrum functions in Fourier space. They are related to each other through kinematic relations for a given type of flow. The real-space correlation functions are the most fundamental quantity and building blocks of statistical theory for any stochastic field. The statistical measures of density field are also a primary focus of many existing literature. This section will introduce/review these fundamental statistical descriptions and relations between different measures, along with results from N-body simulations. Analytical models for these statistical measures are also presented.

#### 3.1 One-point probability distributions of density field

Projecting particle field onto structured grid usually involves information loss and numerical noise. Without projecting onto grid, Delaunay tessellation is used in this section to reconstruct the density field and maximumly preserve information from N-body data. For a particle at location  $\mathbf{x}$ , the particle overdensity  $\delta(\mathbf{x})$  and log-density  $\eta(\mathbf{x})$  are defined as

$$\delta(\mathbf{x}) = \frac{\rho(\mathbf{x})}{\rho_0} - 1 \quad \text{and} \quad \eta(\mathbf{x}) = \log(1 + \delta(\mathbf{x})) = \log\left(\frac{\rho(\mathbf{x})}{\rho_0}\right), \quad (2)$$

where  $\rho(\mathbf{x}) = m_p/V_p$  is a local matter density at comoving coordinate  $\mathbf{x}$ ,  $m_p$  is the particle mass,  $V_p$  is the volume occupied by that particle, and  $\rho_0$  is the mean (comoving) density. In linear theory,  $\eta(\mathbf{x}) \approx \delta(\mathbf{x})$  for small  $\delta(\mathbf{x}) \ll 1$  on large scale. They are different on small scale in the nonlinear regime. Due to normalization that total volume should equal the sum of all particle volume ( $\sum V_p = V$ ), the redshift evolution of distributions of  $\delta$  and  $\eta$  should always satisfy

$$\left\langle \frac{1}{1 + \delta(\mathbf{x})} \right\rangle = 1 \quad \text{and} \quad \langle e^{-\eta(\mathbf{x})} \rangle = 1. \quad (3)$$

Unlike the velocity field, density is not a variable automatically carried by and computed for each particle in N-body simulation. The Delaunay tessellation can be applied to reconstruct the density field from a discrete set of particles (Romano-Díaz & Van De Weygaert 2007; Bernardeau & vandeWeygaert 1996). All particles in system are first connected by a set of non-overlapping tetrahedra (triangles in two-dimension). The volume  $V_p$  that each particle occupies can be determined from the volume of its surrounding tetrahedral. The density  $\rho(\mathbf{x})$  of each particle can be subsequently computed. This enables us to compute density distribution for halo particles and out-of-halo particles separately.

By computing density for each particle from simulation in Section 2, Fig. 1a presents the redshift evolution of one-point density distribution  $\delta(\mathbf{x})$  for all particles in N-body system. Due to gravitational collapse on small scale,  $\delta(\mathbf{x})$  evolves from an initial Gaussian (symmetric) at high redshift to a "double-power-law" distribution (asymmetric and highly skewed toward  $\delta > 0$ ) at  $z=0$  with a long tail  $\propto \delta^{-3}$ . The distribution is approximately  $\propto \delta^{-1}$  for small  $\delta$ .

For comparison, the distribution of density can also be obtained by projecting particles onto structure grid using Cloud-in-Cell (CIC) assignment scheme with a given size of grid ( $\Delta x$ ). Results of (grid-based) density distributions for different  $\Delta x$  are presented in Fig. 1b) with an approximate scaling of  $\propto \delta^{-2}$  that is consistent with literature (Klypin et al. 2018). For grid-based density,  $\langle \delta \rangle = 0$ . Because of the limit of grid resolution, the grid-based density is much smaller than particle density directly obtained from Delaunay tessellation.

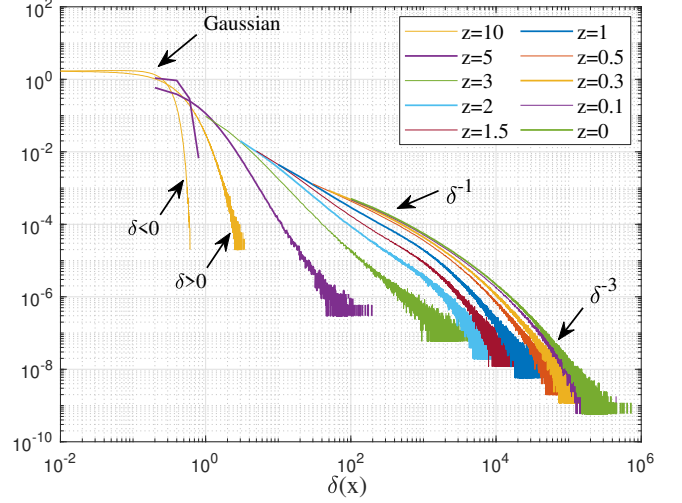


**Figure 1a.** The redshift evolution of density distribution  $\delta$  from  $z=10$  to  $z=0$ . Density evolves from an initial Gaussian to an asymmetric distribution with a long tail  $\propto \delta^{-3}$ . Initial Gaussian distribution at high redshift has two branches ( $\delta > 0$  and  $\delta < 0$ ).

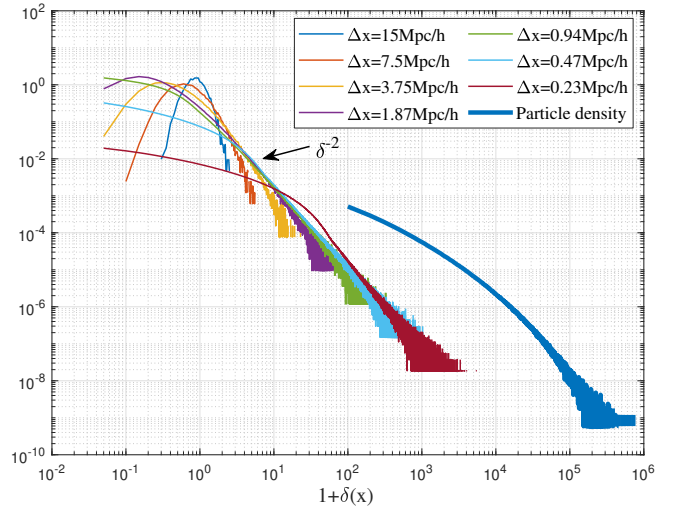


**Figure 1b.** The distribution of  $(1 + \delta)$  obtained by projecting particles onto structured grid with a CIC scheme and different grid size  $\Delta x$  at redshift  $z=0$ . The distribution shows an approximate scaling of  $\propto \delta^{-2}$ . The particle density from Delaunay tessellation is also plotted for comparison with greater density values than grid-based density.

Similarly, Fig. 2 plots the redshift evolution of log-density distribution  $\eta(\mathbf{x})$  from  $z=10$  to  $z=0$ . A bimodal distribution is gradually developed from an initial Gaussian distribution. The first peak corresponds to out-of-halo particles in the low-density region that do not belong to any halos with  $\langle \eta \rangle < 0$ . The second peak comes from all particles residing in halos with higher density and wider dispersion. A simple bimodal equation can be used to fit this distribution,

$$f(\eta) = \frac{c_1}{\sqrt{2\pi}\sigma_1} \exp\left[-\frac{(\eta - \mu_1)^2}{2\sigma_1^2}\right] + \frac{1 - c_1}{\sqrt{2\pi}\sigma_2} \exp\left[-\frac{(\eta - \mu_2)^2}{2\sigma_2^2}\right] \quad (4)$$

with best fitting parameters  $c_1 = 0.404$ ,  $\mu_1 = -0.30$ ,  $\sigma_1 = 1.212$ ,  $\mu_2 = 4.256$ ,  $\sigma_2 = 2.979$  at  $z=0$ . Fitted curve is plotted in the same

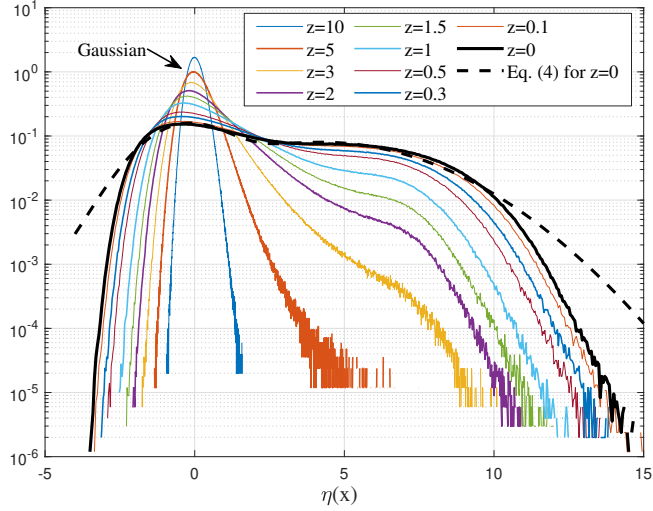


**Figure 2.** Distribution of log-density  $\eta(\mathbf{x})$  at different redshifts  $z$ . The log-density  $\eta(\mathbf{x})$  evolves from a relatively Gaussian to a bimodal distribution at  $z=0$  with two peaks corresponding to halo (60%) and out-of-halo (40%) particles. Inverse mass cascade leads to continuous mass exchange from out-of-halo to halos and the formation of two peaks in density distribution.

figure with about 60% particles in halos and 40% out-of-halo particles. This is consistent with the prediction from inverse mass cascade theory (see Xu 2021a, Eq. (38)), i.e. 60% of total mass is in all halos at  $z = 0$ . There is a continuous exchange of mass from out-of-halo to halos due to inverse mass cascade. Particles in halos should have an average density close to  $\delta = \Delta_c - 1$ , where the critical density ratio  $\Delta_c = 18\pi^2$  from a spherical collapse model or a two-body collapse model (TBCM, Eq. (89) in (Xu 2021d)) such that  $\langle \eta \rangle \approx 5.17$  (close to  $\mu_2$  as the mean density for all halo particles). Figure 2 reflects the effect of inverse mass cascade on density distributions (Xu 2021a,b).

It is also natural to check the density distributions of halo particles and out-of-halo particles separately. By identifying all halos in entire system and dividing all particles into halo and out-of-halo particles, Fig. 3 presents the redshift evolution of distributions of log-density  $\eta(\mathbf{x})$  for halo and out-of-halo particles, respectively. For out-of-halo particles, the distribution of  $\eta$  is relatively Gaussian with mean density decreasing with time. The distribution of  $\delta$  is lognormal for out-of-halo particles that is consistent with Hubble's finding (Hubble 1934). However, for halo particles, the log-density distribution is non-Gaussian and evolves with increasing mean density due to the continuous formation and growth of halos.

To characterize the time evolution of distribution of any random variable  $\tau$ , statistical quantities such as the skewness and kurtosis should be used. A generalized kurtosis  $K_n(\tau)$  is defined as

$$K_n(\tau) = \frac{\langle (\tau - \langle \tau \rangle)^n \rangle}{\langle (\tau - \langle \tau \rangle)^2 \rangle^{n/2}} = \frac{S_n^{cP}(\tau)}{S_2^{cP}(\tau)^{n/2}}, \quad (5)$$

where the central moment of order  $n$  for random variable  $\tau$  reads

$$S_n^{cP}(\tau) = \langle (\tau - \langle \tau \rangle)^n \rangle. \quad (6)$$

The odd order generalized kurtosis should vanish for symmetric distributions. Specifically for Gaussian distribution,  $K_3 = K_5 = 0$ ,  $K_2 = 1$ ,  $K_4 = 3$ ,  $K_6 = 15$ , and  $K_8 = 105$ .

Figure 4 presents the redshift evolution of generalized kurtosis. For out-of-halo particles, the generalized kurtosis ( $K_3(\eta)$  to  $K_6(\eta)$ ) is relatively independent of time. The distribution is relatively Gaussian

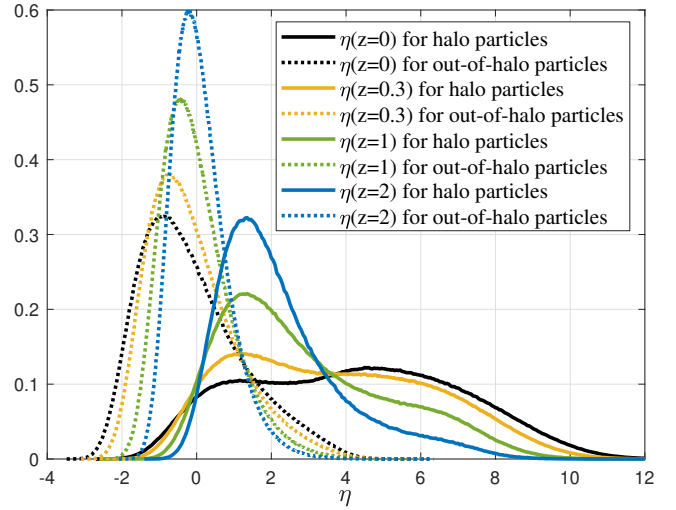


**Figure 3.** Redshift evolution of log-density distributions  $\eta(\mathbf{x})$  for two different types of particles. For out-of-halo particles, distribution is relatively Gaussian with a decreasing and negative mean density due to more out-of-halo particles absorbed into halos. For halo particles, the distribution evolves with an increasing mean log-density.

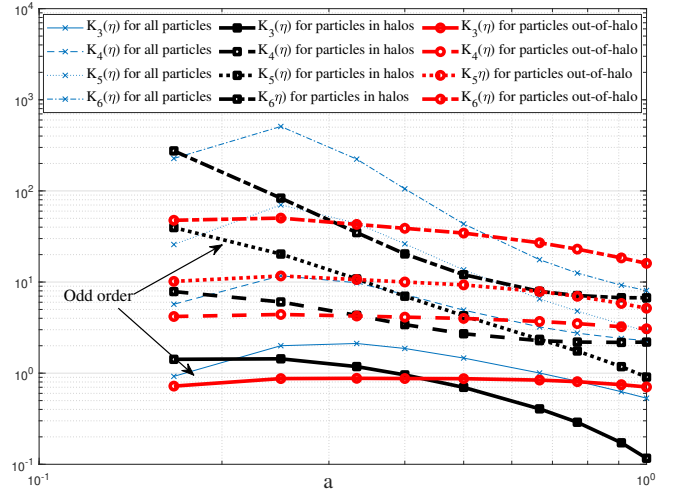


**Figure 4.** The redshift evolution of generalized kurtosis of log-density  $\eta$  for two different types of particles. The density distribution for out-of-halo particles is relatively Gaussian with generalized kurtosis  $K_4 \approx 3$  and  $K_6 \approx 15$  at  $z=0$ . The density distribution for halo particles becomes more symmetric with vanishing odd order generalized kurtosis, while even order kurtosis  $K_4 \rightarrow 2$  and  $K_6 \rightarrow 7$ .

with  $K_4 \approx 3$  and  $K_6 \approx 15$  at  $z=0$ , such that the distribution of  $\delta$  for out-of-halo particles is approximately log-normal. The distribution for halo particles approaches a symmetric distribution with vanishing odd order kurtosis and even order kurtosis  $K_4 \rightarrow 2$  and  $K_6 \rightarrow 7$ .

Figure 5 plots the variation of mean and standard deviation of log-density with time. For out-of-halo particles, the mean log-density decreases with time and  $\langle \eta \rangle < 0$  after  $z=1$  (or  $a=0.5$ ). While the mean log-density of halo particles increase with time, i.e.  $\langle \eta \rangle \propto a^{1/2}$ . The power-law scaling of  $std(\eta) \propto a^{1/2}$  can also be found from this plot, reflecting the fact that spread of halo particle density becomes wider due to continuous mass accretion.



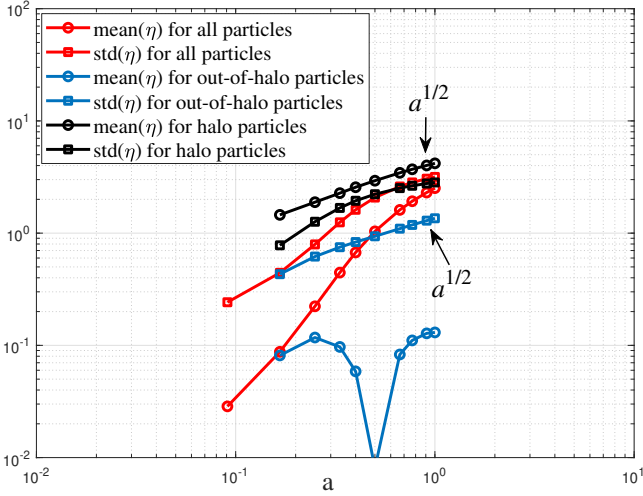


**Figure 5.** The variation of mean and standard deviation of log-density  $\eta(\mathbf{x})$  with scale factor  $a$ . The mean log-density for out-of-halo particles decreases with time and  $\langle \eta \rangle < 0$  after  $z=1$ . The mean log-density of all halo particles increases with time and the standard deviation  $std(\eta) \propto a^{1/2}$ .

### 3.2 Two-point statistical measures of density field

#### 3.2.1 Density correlation from radial distribution function

The gravitational interaction between collisionless particles leads to correlations in particle positions. Following the statistical mechanics of molecular liquid, we start from the radial distribution function  $g(r)$  at a given scale factor  $a$ , a quantity to measure the averaged particle density from an arbitrary reference particle. The number of particles in spherical shell of thickness  $dr$  at a distance  $r$  from the reference particle can be written as:

$$dN_p = g(r) \frac{N_p}{V} 4\pi r^2 dr, \quad (7)$$

where  $N_p/V$  is the mean density of particles,  $N_p$  is the total number of particles in the system, and  $V$  is the volume. The mean comoving density  $\rho_0 = N_p m_p / V$ . The normalization condition reads

$$\int_0^\infty g(r) 4\pi r^2 dr = \frac{N_p - 1}{N_p} V. \quad (8)$$

The two-point second order density correlation function at a given scale factor  $a$  is given by  $\xi(r)$  that can be related to the radial distribution function  $g(r)$  as

$$\xi(r) = \langle \delta(\mathbf{x}) \delta(\mathbf{x} + \mathbf{r}) \rangle = g(r) - 1, \quad (9)$$

with normalization condition,

$$\int_0^\infty \xi(r, a) 4\pi r^2 dr = -V/N_p < 0, \quad (10)$$

such that  $\xi(r, a)$  cannot be positive on all scales. Density must be negatively correlated on some scale  $r$ . Two length scales can be defined from the moments of density correlation (see Fig. 10),

$$l_{\delta 0}(a) = \int_0^\infty \xi(r, a) dr, \quad l_{\delta 1}^2(a) = \int_0^\infty \xi(r, a) r dr. \quad (11)$$

#### 3.2.2 Specific potential/kinetic energy from density correlation

In principle, the specific potential energy (per mass) of any system with particles interacting via a pairwise potential  $V_g(r)$  can be related

to the radial distribution function  $g(r)$  as,

$$PE = \frac{2\pi\rho_0}{m_p^2} \int_0^\infty r^2 [g(r) - 1] V_g(r) dr, \quad (12)$$

where  $\rho_0$  is the mean density. With  $V_g(r) = -Gm_p^2/r$  for gravity, the specific potential energy in physical coordinate reads

$$P_y(a) = -\frac{2\pi G\rho_0}{a} \int_0^\infty \xi(r, a) r dr = -\frac{3H_0^2 l_{\delta 1}^2}{4a} < 0. \quad (13)$$

The specific kinetic energy of entire system can be related to the potential energy via a cosmic energy equation (Irvine 1961; Layzer 1963; Mo et al. 1997)(also see Xu 2022g, Eqs. (2) and (17)), i.e.,

$$\frac{\partial (K_p + P_y)}{\partial t} + H(2K_p + P_y) = 0, \quad (14)$$

with an exact solution of

$$K_p = a^{-2} \int_0^a a P_y da - P_y. \quad (15)$$

Substituting Eq. (13) into (15), the specific kinetic energy can be finally related to the density correlation as (Sheth et al. 2001b),

$$\begin{aligned} K_p &= \frac{3}{4} H_0^2 a^{-1} \left[ \int_0^\infty \xi(r, a) r dr - a^{-1} \int_0^a \left( \int_0^\infty \xi(r, a) r dr \right) da \right] \\ &= \frac{3}{4} H_0^2 a^{-1} \left( l_{\delta 1}^2 - a^{-1} \int_0^a l_{\delta 1}^2 da \right). \end{aligned} \quad (16)$$

The evolution of kinetic and potential energy of N-body system in an expanding background can be modeled by a power law solution that is proportional to time  $t$  (see Xu 2022g, Eq. (40)),

$$K_p = -\varepsilon_u t, \quad P_y = \frac{7}{5} \varepsilon_u t, \quad (17)$$

where the rate of energy cascade  $\varepsilon_u$  is a negative constant,

$$\varepsilon_u = -\frac{3}{2} \frac{\partial u^2}{\partial t} \approx -\frac{3}{2} \frac{u_0^2}{t_0}. \quad (18)$$

The correlation length  $l_{\delta 1}^2$  may be related to the rate of energy cascade as (using Eqs. (13) and (17)),

$$l_{\delta 1}^2(a) = \int_0^\infty \xi(r, a) r dr = -\frac{56}{45} \frac{\varepsilon_u}{H_0^3} a^{5/2}. \quad (19)$$

#### 3.2.3 Density spectrum/dispersion functions and real space distribution of density fluctuation

The density spectrum  $E_\delta(k, a)$  in Fourier space and correlation function  $\xi(r, a)$  in real space are related through a pair of Fourier transformations:

$$E_\delta(k, a) = \frac{2}{\pi} \int_0^\infty \xi(r, a) kr \sin(kr) dr, \quad (20)$$

$$\xi(r, a) = \int_0^\infty E_\delta(k, a) \frac{\sin(kr)}{kr} dk. \quad (21)$$

In Peebles' convention (Peebles 1980), the usual matter power spectrum  $P_\delta(k, a)$  reads

$$P_\delta(k, a) = 2\pi^2 E_\delta(k, a) / k^2. \quad (22)$$

The dimensionless power spectrum  $\Delta_\delta^2(k, a)$  (the power per logarithmic interval) reads

$$\Delta_\delta^2(k, a) = E_\delta(k, a) k. \quad (23)$$

The variance of density fluctuation (density dispersion function), i.e. the density fluctuation contained in all scales above  $r$  should be

$$\sigma_{\delta}^2(r, a) = \int_{-\infty}^{\infty} E_{\delta}(k, a) W(kr)^2 dk, \quad (24)$$

where  $W(x \equiv kr)$  is a window function when smoothed with a filter of size  $r$ . For a typical tophat spherical filter,  $r$  is the radius of filter and the window function is written as

$$W(x) = \frac{3}{x^3} [\sin(x) - x \cos(x)] = 3 \frac{j_1(x)}{x}, \quad (25)$$

where

$$j_1(x) = \frac{\sin(x)}{x^2} - \frac{\cos(x)}{x} \quad (26)$$

is the *first* order spherical Bessel function of the first kind. With  $W(0) = 1$ , the variance of density fluctuation  $\sigma_{\delta}^2(0) \rightarrow \infty$ , i.e. diverging with  $r \rightarrow 0$ .

A relation between  $\xi(r)$  and  $\sigma_{\delta}^2(r)$  for a tophat filter in Eq. (25) can be derived exactly from Eqs. (21) and (24),

$$\xi(2r) = \frac{1}{72r^2} \frac{\partial}{\partial r} \left( \frac{1}{r^2} \frac{\partial}{\partial r} \left( r^3 \frac{\partial}{\partial r} \left( \sigma_{\delta}^2(r) r^4 \right) \right) \right). \quad (27)$$

For a power-law density spectrum  $E_{\delta}(k) \equiv bk^{-m}$ , a power-law correlation is expected,

$$\xi(r) = -2b\Gamma(-m) \sin\left(\frac{m\pi}{2}\right) r^{m-1}, \quad (28)$$

along with a power-law density dispersion function

$$\sigma_{\delta}^2(r) = 72 \cdot 2^m b (1+m)(4+m) \Gamma(-5-m) \sin\left(\frac{m\pi}{2}\right) r^{m-1}. \quad (29)$$

It can be easily verified that Eqs. (28) and (29) satisfy Eq. (27).

Finally, the real-space distribution of density fluctuation between scale  $[r, r+dr]$  can be written as,

$$E_{\delta r}(r) = -\frac{\partial \sigma_{\delta}^2(r)}{\partial r}. \quad (30)$$

This distribution can be related to the density spectrum function as,

$$E_{\delta r}(r) r^2 = -4 \int_0^{\infty} E_{\delta}\left(\frac{x}{r}\right) W(x) W'(x) x dx. \quad (31)$$

The fluctuation distribution in real space  $E_{\delta r}(r)$  is equivalent to and contain the same information as the density spectrum in Fourier space. For a power-law density spectrum,  $E_{\delta}(k) \equiv bk^{-m}$ , the fluctuation distribution function  $E_{\delta r}(r)$  can be exactly related to  $E_{\delta}(k)$  as,

$$E_{\delta r}(r) r^2 = E_{\delta}\left(\frac{x_0}{r}\right) \quad (32)$$

and

$$x_0 = \frac{1}{2} \left[ -72(m^2 - 1)(4+m)\Gamma(-5-m) \sin\left(\frac{m\pi}{2}\right) \right]^{-\frac{1}{m}}.$$

With correlation  $\xi(r)$  fully determined from simulation data, we can translate it into the dispersion function  $\sigma_{\delta}^2(r)$  via Eq. (27), the spectrum function  $E_{\delta}$  via Eq. (20), and the real-space fluctuation distribution  $E_{\delta r}(r)$  via Eq. (30) (See Figs. 7, 8, 11, and 12).

### 3.3 Statistical measures of density from N-body simulation

In this section, second order statistical measures for density are obtained from N-body simulation in Section 2. Algorithms are developed to find all pairs with a given separation  $r$  and computing the average of these statistical measures over all particle pairs with the same separation  $r$ . We first compute the radial distribution function

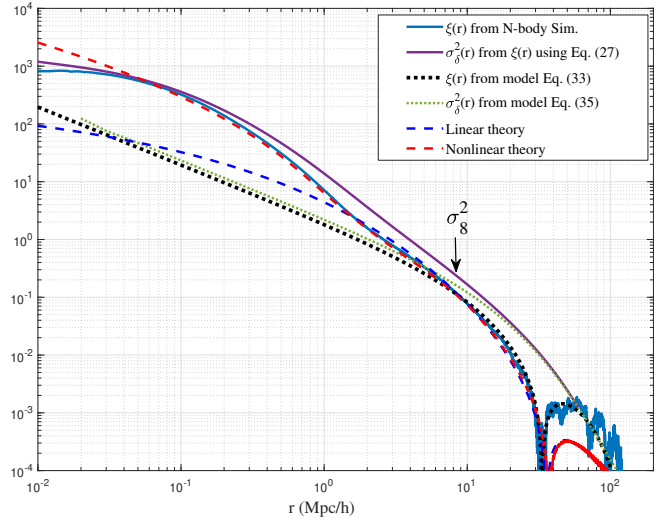


**Figure 6.** Two-point second order density correlation function  $\xi(r)$  (solid blue) varying with scale  $r$  at  $z=0$ . The negative density correlation can be identified for scale larger than  $30\text{Mpc}/h$ . The linear (blue dash) and nonlinear predictions (red dash) are also presented in the same plot and both underestimate the negative correlation. The dispersion function  $\sigma_{\delta}^2(r)$  (solid purple) is obtained from Eq. (27). Models for  $\xi(r)$  and  $\sigma_{\delta}^2(r)$  (Eqs. (33) and (35)) are also presented in the same figure that capture the negative correlation.

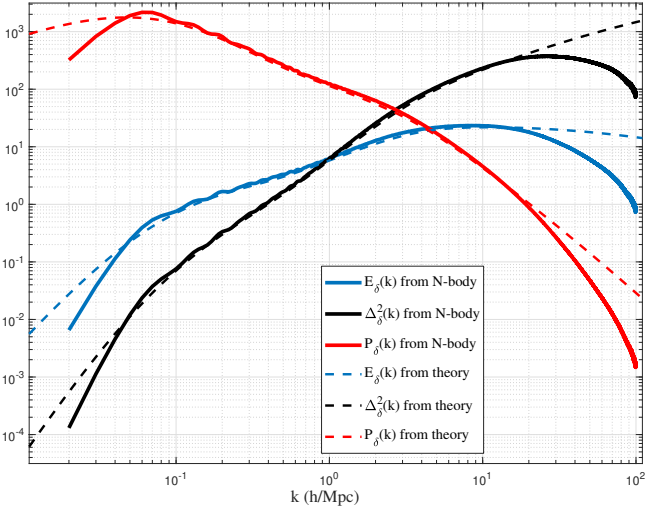
$g(r)$  (Eq. (7)) by counting all pairs at a given distance of  $r$ . Density correlation can be obtained from Eq. (9). In this way, we avoid projecting particle field onto structured grid and maximumly preserve information from N-body simulation.

Figure 6 presents the density correlation function  $\xi(r)$  (using Eq. (9)) at  $z=0$  (solid blue curve). The velocity dispersion  $\sigma_{\delta}^2(r)$  is obtained using Eq. (27) and plotted in solid purple with  $\sigma_{\delta}^2(r = 8\text{Mpc}/h) = \sigma_{\delta}^2$  matching the model input in Table 1. The density correlation  $\xi(r) < 0$  at scale  $r > 30\text{Mpc}/h$ , as required by normalization in Eq. (10). This negative correlation also means a negative mean overdensity (low density void region) and negative reduced velocity dispersion on the same scale (see dynamic relation on large scale Xu 2022f, Eqs. (110), (113) and Fig. 13).

To validate the numerical algorithm identifying particle pairs, we compared with other model predictions (Jenkins et al. 1998). The linear (blue dash) and nonlinear theory prediction (red dash) are both obtained by Fourier transform of the model for density spectrum function (Jenkins et al. 1998). Note that both predictions significantly underestimate the negative density correlation comparing to N-body results (blue solid). Models for  $\xi(r)$  and  $\sigma_{\delta}^2(r)$  in Section 3.4 (Eqs. (33) and (35)) are also plotted (dotted lines) that correctly capture the negative density correlation on large scale.

Similarly, the power spectrum  $E_{\delta}(k)$  can be obtained by Fourier transform (Eq. (20)) of correlation function  $\xi(r)$  that is directly obtained from N-body simulation. Three spectrum functions ( $E_{\delta}(k)$ ,  $P_{\delta}(k)$  from Eq. (22), and  $\Delta_{\delta}^2(k)$  from Eq. (23)) at  $z=0$  are presented in Fig. 7 in solid lines and compared against the nonlinear theory prediction (dash) (Jenkins et al. 1998). Again, the existing theory underestimate the velocity correlation on large scale (or equivalently, small wavenumber  $k$ ).

The density correlation  $\xi(r, a)$  at different redshift  $z$  can be similarly obtained for redshifts between  $z=5$  and  $z=0$  and presented in Fig. 8. The variation of  $\xi(r, a)$  at a given scale  $r$  with scale factor  $a$  is plotted in Fig. 9. The density correlation  $\xi(r, a) \propto a^2$  on large



**Figure 7.** Without projecting particles onto structured grid, density power spectrum  $E_\delta(k)$  ( $Mpc/h$ ),  $P_\delta(k)$  ( $Mpc^3/h^3$ ), and  $\Delta_\delta^2(k)$  (dimensionless) can be obtained from correlation function  $\xi(r)$ . The nonlinear theory predictions (dash lines) are also presented for comparison. The power spectrum  $E_\delta(k)$  was obtained by Fourier transform of correlation function  $\xi(r)$  in Fig. 6 using Eq. (20). Model for  $E_\delta(k)$  is presented in a separate paper (see Xu 2022e, Eq. (132)).

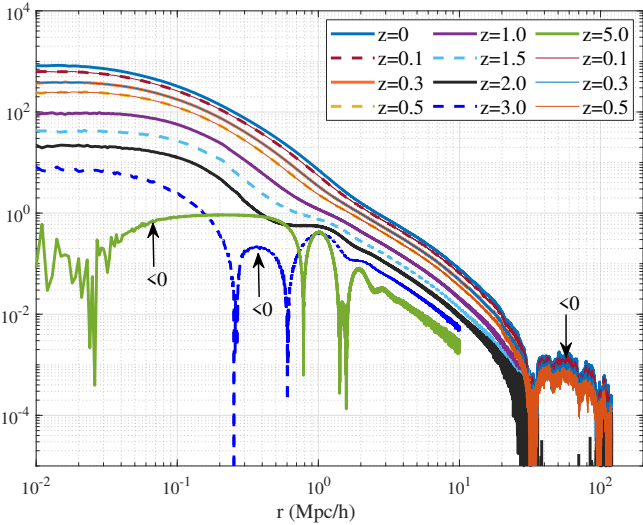


**Figure 8.** Two-point second order density correlation function  $\xi(r, a)$  varying with scale  $r$  at different redshifts  $z=0, 0.1, 0.3, 0.5, 1.0, 1.5, 2.0, 3.0$  and  $5.0$ . Negative density correlation can be identified for  $r > 30 Mpc/h$ .

scale  $r$  that is still in the linear regime, while  $\xi(r, a)$  is approximately  $\propto a^{5/2}$  on small scale  $r$  that is in the nonlinear regime. The variation of two length scales (defined in Eq. (11)) with scale factor  $a$  are plotted in Fig. 10. Two comoving correlation lengths show a limiting scaling of  $l_{\delta 0}(a) \propto a^{5/2}$  and  $l_{\delta 1}(a) \propto a^{5/4}$ . The specific potential energy computed by Eq. (13) using  $l_{\delta 1}$  is in good agreement with the potential energy directly obtained from simulation. Both have a limiting scaling of  $P_y(a) \propto a^{3/2}$  (Eq. (17)).

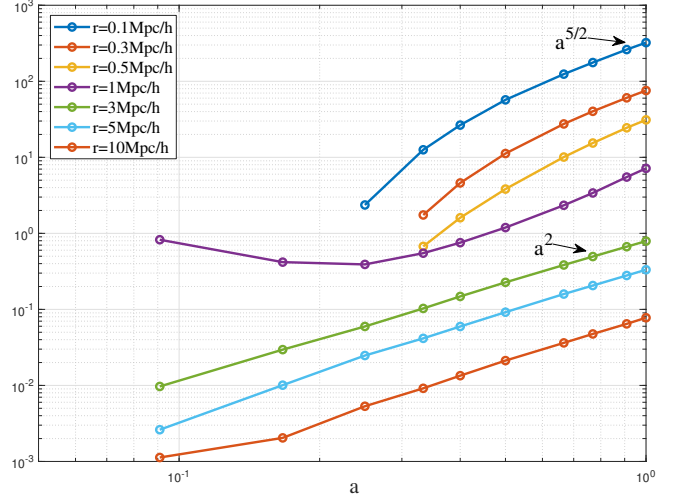


**Figure 9.** Two-point second order density correlation  $\xi(r, a)$  varying with scale factor  $a$  on different scales  $r = 0.1, 0.3, 0.5, 1.0, 3.0, 5.0$  and  $10 Mpc/h$ . The correlation  $\xi(r, a) \propto a^2$  on large scale  $r$  that is in the linear regime, and approximately  $\propto a^{5/2}$  on small scale.

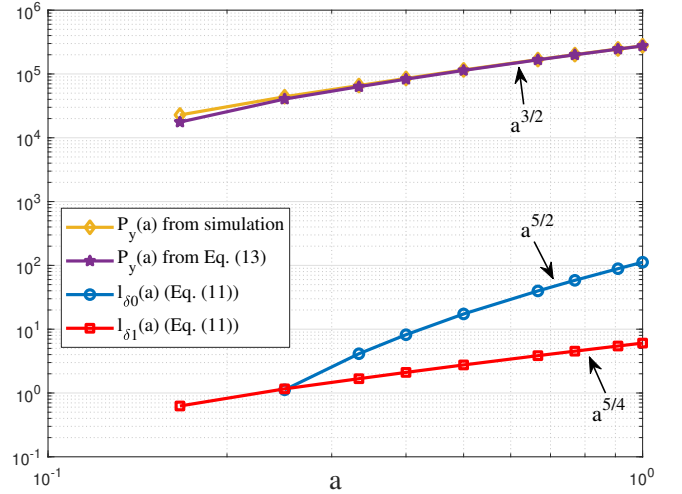


**Figure 10.** The variation of two comoving correlation lengths  $l_{\delta 0}(Mpc/h)$  and  $l_{\delta 1}(Mpc/h)$  with scale factor  $a$ . Both correlation lengths are derived from density correlation  $\xi(r, a)$  (Eq. (11)) with a limiting scaling  $l_{\delta 1}(a) \propto a^{5/4}$  (Eq. (19)) and  $l_{\delta 0}(a) \propto a^{5/2}$ . The potential energy  $P_y(a)$  (in unit of  $(Km/s)^2$ ) using Eq. (13) is in good agreement with  $P_y(a)$  that is directly computed from simulation, both of which show a scaling of  $P_y(a) \propto a^{3/2}$ .

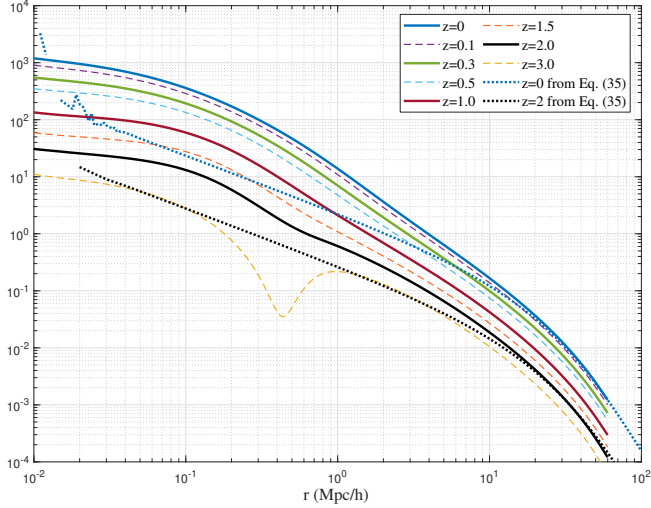
### 3.4 Modeling second order statistical measures of density field

The density correlation on large scale can be analytically derived from velocity correlation functions (see Xu 2022e, Section 5). The exponential correlation for transverse velocity is a direct result of combined kinematics and dynamics on large scale (see Xu 2022f, Section 6.3), which leads to a simple form of density correlation (see Xu 2022e, Eq. (121)),

$$\xi(r, a) = \frac{a_0 u^2 / (r r_2)}{(a H f(\Omega_0))^2} \exp\left(-\frac{r}{r_2}\right) \left[ \left(\frac{r}{r_2}\right)^2 - 7 \left(\frac{r}{r_2}\right) + 8 \right], \quad (33)$$

**Table 2.** Parameters  $a_0(a)$  and velocity dispersion  $u(a)$  ( $km/s$ )

$z$	0	0.1	0.3	0.5	1.0	1.5	2.0	3.0
$a_0(a)$	0.451	0.463	0.486	0.509	0.559	0.604	0.643	0.694
$u(a)$	354.61	335.42	303.37	277.67	231.29	199.76	177.15	148.61

**Figure 11.** Density dispersion function  $\sigma_\delta^2(r)$  at different redshift  $z$  obtained from density correlation  $\xi(r)$  using Eq. (27). Model from Eq. (35) is plotted for comparison with good agreement with simulation data on large scale.

with parameter  $a_0 u^2 = 0.45 u_0^2 a$  and  $u^2(a)$  is the one-dimension velocity dispersion (see Xu 2022e, Fig. 20).

The only comoving length scale in this model  $r_2 = 23.14 Mpc/h$  is independent of time and might be related to the size of sound horizon. Values of  $a_0$  and  $u^2$  are listed in Table 2 for different redshift  $z$ . Obviously  $a_0 u^2 \propto a$  is consistent with the scaling  $\xi(r, a) \propto a^2$  in the linear theory. The correlation turns to negative at  $0.5(7 - \sqrt{17})r_2 \approx 33 Mpc/h$  from Eq. (33). The model of Eq. (33) is also plotted in Fig. 6 that matches the N-body simulation on large scale.

The average correlation  $\bar{\xi}(r, a)$  on large scale should read,

$$\begin{aligned} \bar{\xi}(r, a) &= \frac{3}{r^3} \int_0^r \xi(y, a) y^2 dy \\ &= \frac{a_0 u^2}{(aHf(\Omega_0))^2} \frac{3}{rr_2} \exp\left(-\frac{r}{r_2}\right) \left(4 - \frac{r}{r_2}\right), \end{aligned} \quad (34)$$

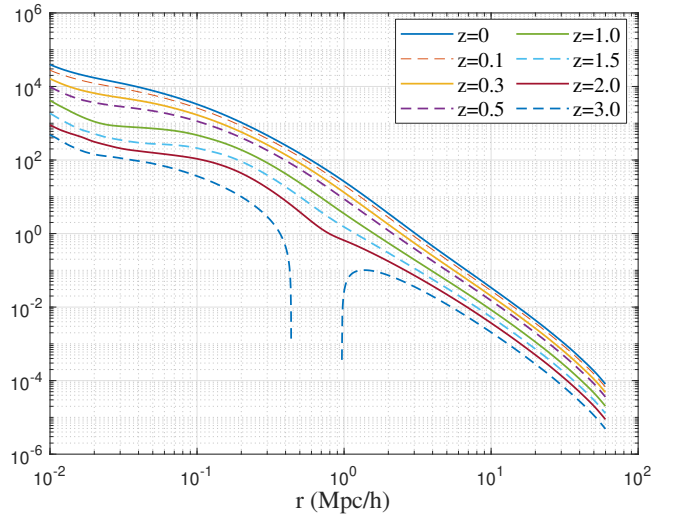
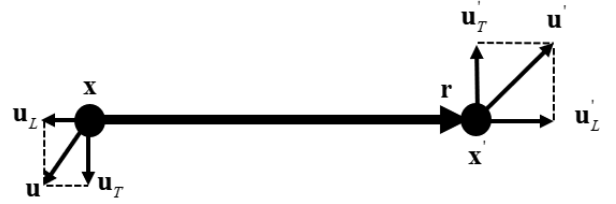
that can be related to the mean pairwise velocity via pair conservation equation (Eq. (41)).

The density dispersion function  $\sigma_\delta^2(r)$  for density fluctuation can be obtained using Eqs. (27) and (33),

$$\begin{aligned} \sigma_\delta^2(r) &= \frac{1}{(aHf(\Omega_0))^2} \cdot \frac{9a_0 u^2}{2r^2} \left\{ 3 \left(\frac{r_2}{r}\right)^4 + \left(\frac{r_2}{r}\right)^2 \right. \\ &\quad \left. - \exp\left(-\frac{2r}{r_2}\right) \left[ 1 + \left(\frac{r_2}{r}\right)^2 \right] \left[ 3 \left(\frac{r_2}{r}\right)^2 + 6 \left(\frac{r_2}{r}\right) + 4 \right] \right\}, \end{aligned} \quad (35)$$

where  $\sigma_\delta^2(r) \propto a^2 r^{-4}$  for large  $r \rightarrow \infty$  and  $\sigma_\delta^2(r) \propto a^2 r^{-1}$  for  $r \rightarrow 0$ . Figure 11 plots the variation of  $\sigma_\delta^2(r)$  obtained from  $\xi(r)$  at different redshifts  $z$ , along with the model in Eq. (35) for comparison.

The real-space distribution of density fluctuation, i.e. function  $E_{\delta r}(r)$  can be subsequently obtained from  $\sigma_\delta^2(r)$  (Eq. (30)) and presented in Fig. 12. The density fluctuation increases with time on

**Figure 12.** Real-space distribution of density fluctuation  $E_{\delta r}(r)$  ( $h/Mpc$ ) on scale  $r$  obtained from density dispersion function  $\sigma_\delta^2(r)$  using Eq. (30). Density fluctuation increases with time on all scales, while fluctuation on small scale increases faster than large scale.**Figure 13.** Longitudinal and transverse velocities on scale  $r$ .

all scales, while kinetic energy decreases on large scale and increase on small scale (see Xu 2022e, Fig. 11).

#### 4 CHARACTERIZING PROBABILITY DISTRIBUTIONS OF VELOCITY FIELDS

The nature of velocity distributions is studied in this section. To understand how velocity distributions vary with scale  $r$  and redshift  $z$ , we are interested in three types of velocities on different scale  $r$ , i.e. the longitudinal velocity  $u_L$  or  $u'_L$ , velocity difference (or pairwise velocity)  $\Delta u_L = u'_L - u_L$ , and velocity sum  $\Sigma u_L = u_L + u'_L$ . For a pair of particles with velocities  $\mathbf{u}, \mathbf{u}'$ , and separation vector  $\mathbf{r} = \mathbf{x}' - \mathbf{x}$ , the longitudinal and transverse velocities read (Fig. 13),

$$\begin{aligned} u_L &= \mathbf{u} \cdot \hat{\mathbf{r}} \quad \text{and} \quad \mathbf{u}_T = -(\mathbf{u} \times \hat{\mathbf{r}} \times \hat{\mathbf{r}}) = \mathbf{u} - (\mathbf{u} \cdot \hat{\mathbf{r}}) \hat{\mathbf{r}}, \\ u'_L &= \mathbf{u}' \cdot \hat{\mathbf{r}} \quad \text{and} \quad \mathbf{u}'_T = -(\mathbf{u}' \times \hat{\mathbf{r}} \times \hat{\mathbf{r}}) = \mathbf{u}' - (\mathbf{u}' \cdot \hat{\mathbf{r}}) \hat{\mathbf{r}}, \end{aligned} \quad (36)$$

where  $\hat{\mathbf{r}} = \mathbf{r}/r$  is the normalized unit vector. For any given scale  $r$ , all particle pairs with a separation between  $r$  and  $r+dr$  ( $dr = 0.001 Mpc/h$  in this work) are identified and the particle position and velocity are recorded to compute the velocity distribution and associated statistical quantities by averaging that quantity over all pairs on the same scale  $r$ . By this way, information is maximumly preserved without projecting particle velocity onto structured grid.



In addition to three velocities that are scale dependent, we are also interested in the distribution of four velocities, i.e. the velocity of all particles in entire system ( $\mathbf{u}_p$ ), velocity of all halo particles ( $\mathbf{u}_{hp}$ ), velocity of all out-of-halo particles ( $\mathbf{u}_{op}$ ), and velocity of all halos identified in the system ( $\mathbf{u}_h$ , the mean velocity of all particles in the same halo). The distributions of these velocities are not scale dependent, but redshift dependent. The redshift evolution of these distributions will significantly improve our understanding of velocity field in dark matter flow.

#### 4.1 Generalized kurtosis, moments, and structure functions

Just like the density distributions in Section 3.1, velocity distributions can be best characterized by generalized kurtosis in Eqs. (5) and (6). The first example is the generalized kurtosis for velocity difference  $\Delta u_L$  (pairwise velocity),

$$K_n(\Delta u_L, r) = \frac{\langle (\Delta u_L - \langle \Delta u_L \rangle)^n \rangle}{\langle (\Delta u_L - \langle \Delta u_L \rangle)^2 \rangle^{n/2}} = \frac{S_n^{cP}(\Delta u_L, r)}{S_2^{cP}(\Delta u_L, r)^{n/2}}, \quad (37)$$

where the central moment of order  $n$  for  $\Delta u_L$  reads

$$S_n^{cP}(\Delta u_L, r) = \langle (\Delta u_L - \langle \Delta u_L \rangle)^n \rangle. \quad (38)$$

The  $n$ th order longitudinal structure function of  $\Delta u_L$  is defined as,

$$S_n^{lP}(r) = \langle (\Delta u_L)^n \rangle = \langle (u'_L - u_L)^n \rangle, \quad (39)$$

**Remarks:** For incompressible hydrodynamics,  $\langle u_L \rangle = \langle \Delta u_L \rangle = \langle \Sigma u_L \rangle = 0$  on all scales of  $r$  and  $S_n^{cP}(\Delta u_L, r) = S_n^{lP}(r)$ , namely the central moment of  $\Delta u_L$  equals the structure function defined in Eq. (39). For self-gravitating collisionless dark matter flow (SG-CFD), two particles tend to approach each other under gravity that leads to a non-zero longitudinal velocity  $\langle u_L \rangle = -\langle \Delta u_L \rangle / 2 > 0$ , and central moment  $S_n^{cP}(\Delta u_L, r) \neq S_n^{lP}(r)$  for SG-CFD. Due to symmetry,  $\langle \Sigma u_L \rangle = 0$  and the distribution of  $\Sigma u_L$  is always symmetric on all scale  $r$  with vanishing odd moments.

#### 4.2 Generalized kurtosis of velocity from N-body simulation

Figure 14 presents the time variation of generalized kurtosis for velocity  $\mathbf{u}_p$  (for all particles),  $\mathbf{u}_{hp}$  (for halo particles), and  $\mathbf{u}_{op}$  (for out-of-halo particles). Different order of kurtosis for Gaussian distribution is plotted as green dash lines for comparison. All velocities are initially Gaussian. The velocity distribution of halo particles  $\mathbf{u}_{hp}$  deviates from Gaussian much faster than the distribution of out-of-halo particles  $\mathbf{u}_{op}$  due to stronger gravitational interaction in halos than gravity between halos. All velocities become non-Gaussian with time to maximize system entropy (Xu 2021c).

Figure 15 plots the even order generalized kurtosis ( $4^{th}$  order – bottom,  $6^{th}$  order – middle, and  $8^{th}$  order – top) of three velocities ( $u_L$ ,  $\Delta u_L$ , and  $\Sigma u_L$ ) at  $z=0$ . The 4th, 6th and 8th kurtosis of Gaussian distribution are also plotted in the same figure with  $K_4 = 3$ ,  $K_6 = 15$ , and  $K_8 = 105$ . Clearly, distributions of three velocities are non-Gaussian on all scales due to the long-range nature of gravity. This is important as it poses serious challenges on any theory that assumes the Gaussianity of velocity fields. Velocity field of fully developed self-gravitating collisionless dark matter flow (SG-CFD) is not Gaussian on any scale despite that they can be initially Gaussian. By contrast, for incompressible hydrodynamics with short range interactions, the distribution of  $u_L$  is nearly Gaussian on large scale and  $\Delta u_L$  is also Gaussian on large scale and only becomes non-Gaussian on small scale due to strong viscous force.

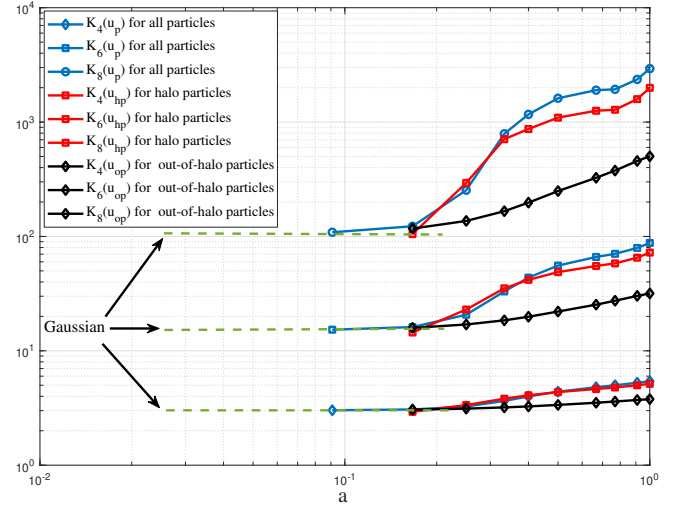


**Figure 14.** Redshift evolution of generalized kurtosis for velocity of all particles (blue), all halo particles (red), and all out-of-halo particles (black). Gaussian distribution is presented as green dash lines. All velocities quickly become non-Gaussian with time to maximize system entropy, while the evolution of out-of-halo particle velocity is at a much slower pace than that of halo particles due to weak gravity on large scale.

In Fig. 15, distribution of  $\Sigma u_L$  approaches the distribution of  $u_L$  on small scale with a limiting correlation (between  $u_L$  and  $u'_L$ ), where  $\rho_L = \langle u'_L u_L \rangle / \langle u_L^2 \rangle = 0.5$  between two velocities (see Xu 2022e, Fig. 16). This is expected as  $r \rightarrow 0$ , the sum velocity  $\lim_{r \rightarrow 0} \Sigma u_L = \lim_{r \rightarrow 0} (u'_L(\mathbf{x}') + u_L(\mathbf{x}))$  will become the total velocity  $\mathbf{u}(\mathbf{x})$  at location  $\mathbf{x}$ . Longitudinal velocities  $u_L$  and  $u'_L$  along many different directions will simply collapse into  $\mathbf{u}(\mathbf{x})$  and this also requires  $\rho_L = 0.5$ , i.e.

$$\begin{aligned} \lim_{r \rightarrow 0} \langle (u'_L + u_L)^2 \rangle &= \lim_{r \rightarrow 0} (\langle u_L'^2 \rangle + \langle u_L^2 \rangle + 2\langle u'_L u_L \rangle) \\ &= \lim_{r \rightarrow 0} |\mathbf{u}(\mathbf{x})|^2 = 3 \lim_{r \rightarrow 0} \langle u_L^2 \rangle. \end{aligned} \quad (40)$$

On large scale, the distribution of  $\Sigma u_L$  approaches the distribution of  $\Delta u_L$  with correlation  $\rho_L = 0$  between  $u_L$  and  $u'_L$ . This is also expected as the sum and difference of two independent random variables with symmetric distribution should follow the same distribution. Finally, on both small and large scales, generalized kurtosis approaches constant such that there exist unique (limiting) probability distributions that are independent of scale  $r$  when  $r \rightarrow 0$  or  $r \rightarrow \infty$ . While on the intermediate scale around  $1 \text{ Mpc}/h$ , all three velocity distributions exhibit the greatest value for generalized kurtosis of different order.

Figure 16 plots the variation of odd order generalized kurtosis ( $K_3(\Delta u_L, r)$  and  $K_5(\Delta u_L, r)$ ) with scale  $r$  at  $z=0$ . The third order kurtosis  $K_3(\Delta u_L, r)$  (skewness) vanishes on both small and large scales, where the distribution of  $\Delta u_L$  is symmetric. The skewness  $K_3(\Delta u_L, r) < 0$  on the intermediate scale (the distribution of  $\Delta u_L$  skews toward positive side, see Fig. 26). The negative skewness can be an important signature of inverse cascade of kinetic energy across halo mass scales (Xu 2021f).

#### 4.3 First moment of velocity and pair conservation equation

While the generalized kurtosis can be used to characterize distributions of different velocities, the moments of velocity distributions can

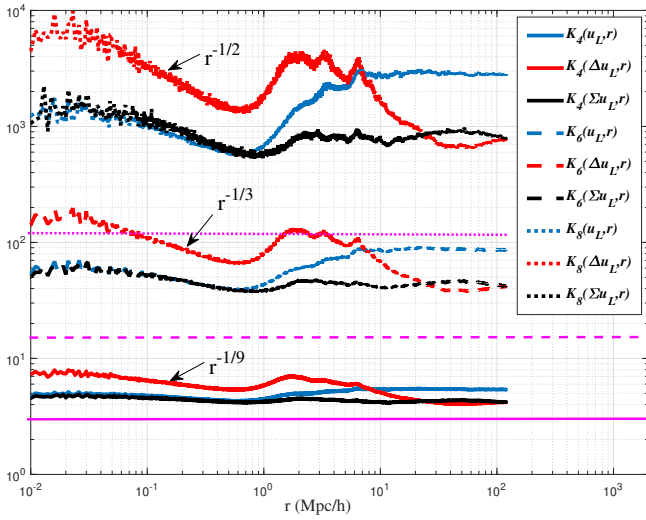


**Figure 15.** The generalized kurtosis ( $4^{th}$ ,  $6^{th}$ , and  $8^{th}$  order) of three velocities varying with scale  $r$  at  $z=0$ . The generalized kurtosis of Gaussian distribution is plotted in the same figure (magenta) for comparison. All velocity distributions are non-Gaussian on all scales due to the long-range gravitational interaction, despite that they can be initially Gaussian. The distribution of  $\Sigma u_L$  approaches that of  $u_L$  on small scale, while the distribution of  $\Sigma u_L$  approaches that of  $\Delta u_L$  on large scale. There exist limiting probability distributions for all velocities on both ends of small and large scales.

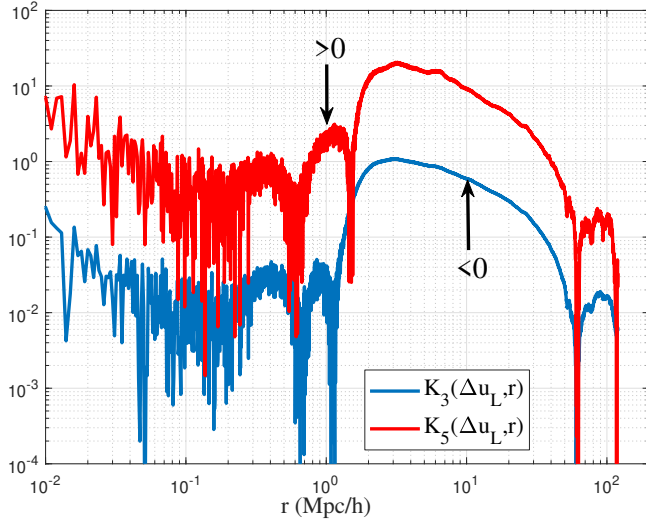


**Figure 16.** The odd order generalized kurtosis of pairwise velocity  $\Delta u_L$  varying with scale  $r$  at  $z=0$ . The third order kurtosis  $K_3(\Delta u_L, r)$  (skewness) vanishes on both small and large scales, where distribution of  $\Delta u_L$  is symmetric. The skewness  $K_3(\Delta u_L, r) < 0$  on the intermediate scale (distribution skews toward positive side). This negative skewness on the intermediate scale should be a result of inverse cascade of kinetic energy.

be studied in detail to provide more insights. To validate the algorithm identifying pairs from N-body simulation, the mean pairwise velocity (first moment) on all scales can be compared against pair conservation equation that relates the pairwise velocity with density correlation (Peebles 1980),

$$\frac{\langle \Delta u_L \rangle}{Har} = -\frac{(1 + \bar{\xi}(r, a))}{3(1 + \xi(r, a))} \frac{\partial \ln(1 + \bar{\xi}(r, a))}{\partial \ln a}, \quad (41)$$

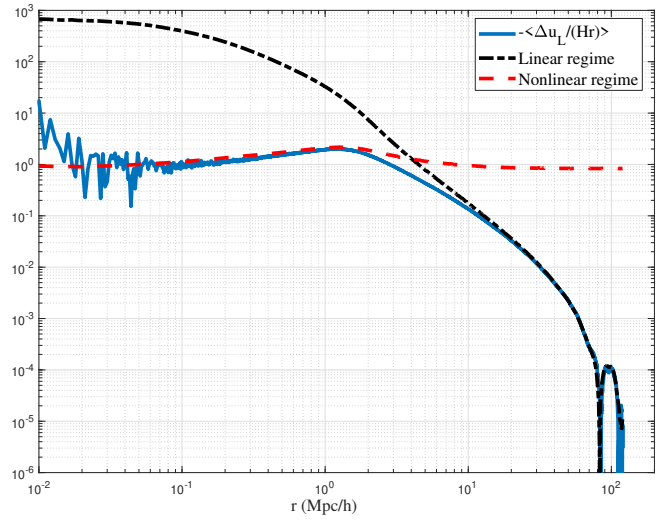


**Figure 17.** The variation of first moment of pairwise velocity  $S_1^P(r) = \langle \Delta u_L \rangle$  (mean pairwise velocity) with scale  $r$  at  $z=0$  (normalized by Hubble constant  $H$ ) from N-body simulation (blue solid). Results are compared with predictions using pair conservation equation for both linear (black dash from Eq. (42)) and nonlinear regime (red dash from Eq. (43)). Predictions are made with density correlation  $\xi(r)$  from N-body simulation.

where  $\bar{\xi}(r, a) = 3r^{-3} \int_0^r \xi(y, a) y^2 dy$  is the volume averaged correlation function (model provided in Eq. (34) for large scale). For linear regime,  $\bar{\xi} \ll 1$  and  $\partial \ln \bar{\xi} / \partial \ln a = 2$ , we have

$$\frac{\langle \Delta u_L \rangle}{Har} = -\frac{2\bar{\xi}(r, a)(1 + \bar{\xi}(r, a))}{3(1 + \xi(r, a))} \approx -\frac{2}{3}\bar{\xi}(r, a). \quad (42)$$

For nonlinear regime with  $\bar{\xi} \gg 1$  and assuming the scaling with scale factor as  $\xi(r, a) \propto a^\alpha$  (Fig. 9) and  $\partial \ln \bar{\xi} / \partial \ln a = \alpha$ , the pair conservation Eq. (41) reduces to,

$$\frac{\langle \Delta u_L \rangle}{Har} = -\frac{\alpha(1 + \bar{\xi}(r, a))}{3(1 + \xi(r, a))}. \quad (43)$$

On small scale, if stable clustering hypothesis ( $\langle \Delta u_L \rangle = -Har$  that is demonstrated in (Xu 2021d)) is assumed combined with a self-similar gravitational clustering with  $\xi(r, a) \propto a^\alpha r^\gamma$ , we have

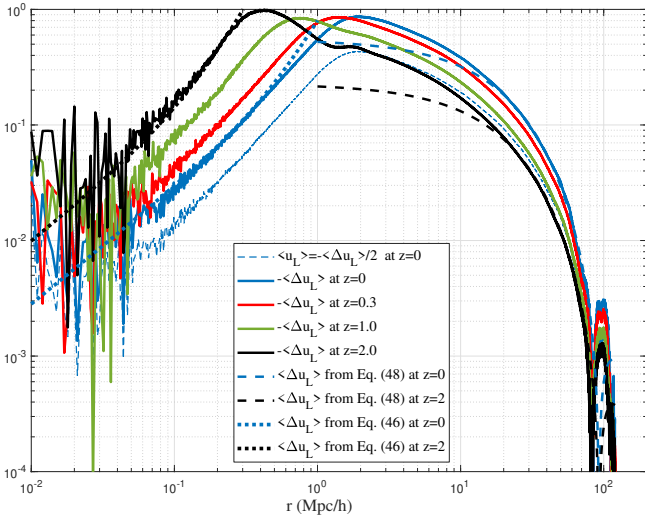
$$\frac{\langle \Delta u_L \rangle}{Har} = -1 \quad \text{and} \quad \alpha = \gamma + 3 \quad (44)$$

Figure 17 plots the variation of the first moment  $S_1^P(r) = \langle \Delta u_L \rangle$  (mean pairwise velocity) with scale  $r$  (normalized by Hubble constant) at  $z=0$ . Results are compared with the prediction from pair conservation equation for both linear (black dash from Eq. (42)) and nonlinear regime (red dash from Eq. (43) with  $\alpha = 5/2$  from Fig. 9) using the density correlation  $\xi(r, a)$  obtained from N-body simulation (Fig. 8). Blue line is the normalized pairwise velocity computed directly from simulation by identifying all particle pairs and associated velocities. Good match with pair conservation equation validates our numerical implementation.

On small scale, an exact expression can be identified from stable clustering hypothesis (also analytically demonstrated by a two-body collapse model in (Xu 2021d)),

$$\langle \Delta u_L \rangle = -Har \quad \text{and} \quad \langle u_L \rangle = Har/2. \quad (45)$$

For nonlinear regime below a characteristic scale  $r_t = 1.3a^{1/2} Mpc/h$  where the longitudinal velocity correlation equals



**Figure 18.** Mean (first moment) longitudinal velocity  $\langle u_L \rangle$  and velocity difference (pairwise velocity)  $|\langle \Delta u_L \rangle|$  varying with scale  $r$  at different redshift  $z$ , normalized by velocity dispersion  $u(a)$ . Note that  $\langle \Delta u_L \rangle = -2\langle u_L \rangle$  is not zero, while  $\langle u_L \rangle = -\langle u'_L \rangle$  and velocity sum  $\langle \Sigma u_L \rangle = 0$  on all scales. For SG-CFD, the velocity field  $\mathbf{u}$  and vector  $\mathbf{r}$  between two particles are correlated that leads to a nonzero longitudinal velocity  $\langle u_L \rangle = \langle \mathbf{u} \cdot \mathbf{r} \rangle > 0$ .

the transverse velocity correlation (see Xu 2022e, Figs. 3 and 4), a better relation to fit the simulation data reads

$$\langle \Delta u_L \rangle = -Har - ua^{-5/3} \left( \frac{r}{r_t} \right)^{5/2}, \quad (46)$$

where  $u(a)$  is one-dimension velocity dispersion in Table 2. On large scale, from pair conservation Eq. (42), the mean pairwise velocity can be written as

$$\langle \Delta u_L \rangle \approx -\frac{2}{3} Har \bar{\xi}(r, a) = -\frac{2Ha}{r^2} \int_0^r \xi(y) y^2 dy. \quad (47)$$

With Eq. (34) for mean correlation  $\bar{\xi}(r, a)$ , the mean pairwise velocity is simply the derivative of velocity correlation  $R_2 = \langle \mathbf{u} \cdot \mathbf{u}' \rangle$  (see Xu 2022e, Eq. (120)), we should have

$$\langle \Delta u_L \rangle = \frac{2}{aHf(\Omega_0)} \frac{\partial R_2}{\partial r} = \frac{2a_0 u^2}{aHr_2} \exp\left(-\frac{r}{r_2}\right) \left(\frac{r}{r_2} - 4\right). \quad (48)$$

Figure 18 plots the mean longitudinal velocity  $\langle u_L \rangle$  and velocity difference  $-\langle \Delta u_L \rangle$  at different redshift  $z$ . Note that  $\langle \Delta u_L \rangle = -2\langle u_L \rangle$  vanishes on both small and large scales. Since  $\langle u_L \rangle = -\langle u'_L \rangle$ , mean velocity sum  $\langle \Sigma u_L \rangle = 0$  on all scales.  $\langle u_L \rangle > 0$  and  $\langle \Delta u_L \rangle < 0$  indicate that two particles are moving toward each other due to gravity. By contrast,  $\langle u_L \rangle = \langle \Delta u_L \rangle = \langle \Sigma u_L \rangle = 0$  on all scales for incompressible collisional hydrodynamics, where  $\mathbf{u}$  and  $\mathbf{r}$  are independent of each other. Models for pairwise velocity on small and large scales (Eqs. (46) and (48)) are also presented for comparison. The entire range of  $\langle \Delta u_L \rangle$  can be modeled by smoothly connecting two models on small and large scales (see Xu 2022e, Eq. (147)).

#### 4.4 Second moment of velocity field

Figure 19 plots the second moments and central moments (normalized by  $u^2$ ) of three velocities  $u_L$ ,  $\Delta u_L$ , and  $\Sigma u_L$  on all scales at  $z=0$ . The longitudinal velocities ( $u_L$  and  $u'_L$ ) must be strongly correlated

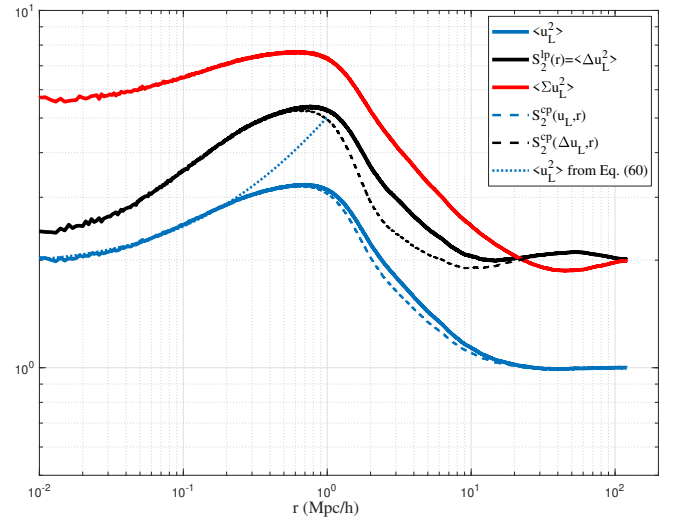


**Figure 19.** The variation of second moments of  $\langle u_L^2 \rangle$ ,  $\langle \Delta u_L^2 \rangle$  and  $\langle \Sigma u_L^2 \rangle$  at  $z=0$ , normalized by velocity dispersion  $u_0^2$  of entire system. On small scale,  $\langle \Delta u_L^2 \rangle = \langle u_L^2 \rangle = \langle \Sigma u_L^2 \rangle / 3 = 2u^2$  and on large scale  $\langle \Delta u_L^2 \rangle = \langle \Sigma u_L^2 \rangle = 2\langle u_L^2 \rangle = 2u^2$ . The difference between the second order longitudinal structure function  $S_2^{IP}(r) = \langle \Delta u_L^2 \rangle$  and central moment  $S_2^{CP}(\Delta u_L, r)$  is due to the nonzero  $\langle \Delta u_L \rangle$  on intermediate scale. By contrast,  $S_2^{IP} = S_2^{CP}$  and  $\langle u_L^2 \rangle = u^2$  on all scales for incompressible hydrodynamics. Model for longitudinal dispersion  $\langle u_L^2 \rangle$  in Eq. (60) is also plotted (dotted line).

on small scale due to gravitational interaction and uncorrelated on large scale. The correlation between  $u_L$  and  $u'_L$  leads to

$$\langle \Delta u_L^2 \rangle = 2\langle u_L^2 \rangle (1 - \rho_L), \quad \langle \Sigma u_L^2 \rangle = 2\langle u_L^2 \rangle (1 + \rho_L), \quad (49)$$

where  $\rho_L$  is the correlation coefficient between  $u_L$  and  $u'_L$ . On small scale,  $\rho_L = 1/2$  for  $r \rightarrow 0$  (Eq. (40)). Pairs in small halos are fully correlated, while pairs in large halos are uncorrelated, such that the average correlation is around 1/2 (see Xu 2022e, Section 3.3),

$$\langle \Delta u_L^2 \rangle = \langle u_L^2 \rangle = \langle \Sigma u_L^2 \rangle / 3 = 2u^2. \quad (50)$$

On large scale with  $\rho_L = 0$  for  $r \rightarrow \infty$ ,

$$\langle \Delta u_L^2 \rangle = \langle \Sigma u_L^2 \rangle = 2\langle u_L^2 \rangle = 2u^2. \quad (51)$$

By contrast, the incompressible collisional hydrodynamics should have  $\langle \Delta u_L^2 \rangle = 0$  and  $\langle \Sigma u_L^2 \rangle = 4$  on small scale with  $\rho_L = 1$  when  $r \rightarrow 0$ , and  $\langle u_L^2 \rangle = u^2$  on all scales.

The difference between second moments and the central moments of  $u_L$  and  $\Delta u_L$  on intermediate scale is due to the non-zero first moment  $\langle u_L \rangle$  and  $\langle \Delta u_L \rangle$ , as shown in Fig. 19. All second moments increase with  $r$  initially and decrease for  $r > r_t$ . Model for  $\langle u_L^2 \rangle$  on small scale is proposed in Eq. (60), while model for  $\langle u_L^2 \rangle$  on large scale is proposed in our previous work (see Xu 2022e, Eq. (136)).

By identifying all pairs of particles with different separation  $r$ , we can compute the variance of velocity on different scales  $r$ , namely the total variance  $\langle u^2 \rangle = \langle \mathbf{u} \cdot \mathbf{u} \rangle$ , the longitudinal variance  $\langle u_L^2 \rangle$ , and the transverse variance  $\langle u_T^2 \rangle = \langle \mathbf{u}_T \cdot \mathbf{u}_T \rangle$ , where

$$\langle u^2 \rangle = \langle \mathbf{u} \cdot \mathbf{u} \rangle = \langle u_L^2 \rangle + \langle \mathbf{u}_T \cdot \mathbf{u}_T \rangle. \quad (52)$$

Figure 20 plots three velocity dispersions  $\langle u^2 \rangle$ ,  $\langle u_L^2 \rangle$ , and  $\langle u_T^2 \rangle$  on different scale  $r$  at  $z=0$ . The initial increase of all three dispersions

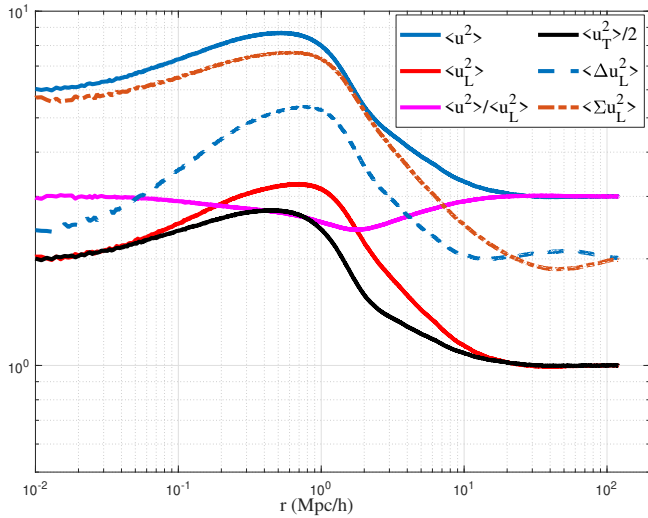


**Figure 20.** The variation of velocity dispersions  $\langle u^2 \rangle = \langle \mathbf{u} \cdot \mathbf{u} \rangle$ ,  $\langle u_L^2 \rangle$ , and  $\langle u_T^2 \rangle = \langle \mathbf{u}_T \cdot \mathbf{u}_T \rangle$  with scale  $r$  at  $z=0$  (normalized by  $u_0^2$ ). The initial increase of all dispersions with  $r$  for  $r < r_t$  is mostly due to the increasing velocity dispersion with halo size on small scale. With more pairs of particles from different halos on larger scale  $r > r_t$ , dispersion starts to decrease with  $r$ . With all pairs of particles from different halos, velocity dispersion reaches a plateau with  $\langle u^2 \rangle = 3\langle u_L^2 \rangle = 3u^2$ . The variation of  $\langle u^2 \rangle$  can be related to density correlation  $\xi(r)$  through dynamic relations on large scale (see Xu 2022f, Eq. (113)).

with  $r$  for  $r < r_t$  (pair of particles are more likely from same halos) is mostly due to the increase of velocity dispersion with halo size. With more pairs of particles from different halos for scale  $r > r_t$ , the velocity dispersions sharply decrease with  $r$ . At some large scale  $r$ , almost all pair of particles are from different halos, where velocity dispersions reach a plateau with  $\langle u^2 \rangle = 3\langle u_L^2 \rangle = 3u^2$ . The variation of  $\langle u^2 \rangle$  can be related to density correlation  $\xi(r)$  through dynamic relations on large scale (see Xu 2022f, Eq. (113))

For particle pairs separated by scale  $r$ , the second moments of longitudinal and transverse velocities are comparable on both small and large scales. However,  $\langle u_L^2 \rangle > \langle u_T^2 \rangle/2$  on intermediate scales with  $\langle u_L^2 \rangle > \langle u^2 \rangle/3$ , i.e. energy is not equipartitioned on intermediate scale. The velocity dispersion on small scale  $\langle u_L^2 \rangle|_{r=0} \approx 2 \langle u_L^2 \rangle|_{r=\infty}$ , i.e. the kinetic energy on small scale is twice of the kinetic energy on large scale.

The variation of pairwise velocity dispersion (or the second order longitudinal structure function)

$$S_2^{lp} = \langle (\Delta u_L)^2 \rangle = \left\langle \left( u'_L - u_L \right)^2 \right\rangle \quad (53)$$

and velocity sum

$$\left\langle \left( \sum u_L \right)^2 \right\rangle = \left\langle \left( u'_L + u_L \right)^2 \right\rangle$$

are also plotted in the same figure for comparison.

#### 4.5 Two-thirds law for even order moments of pairwise velocity

Now we focus on the second order structure function  $S_2^{lp}$  (pairwise velocity dispersion in Eqs. (39) and (53)) that is defined as

$$S_2^{lp}(r) = \langle (\Delta u_L)^2 \rangle = 2 \left( \langle u_L^2 \rangle - L_2(r) \right), \quad (54)$$

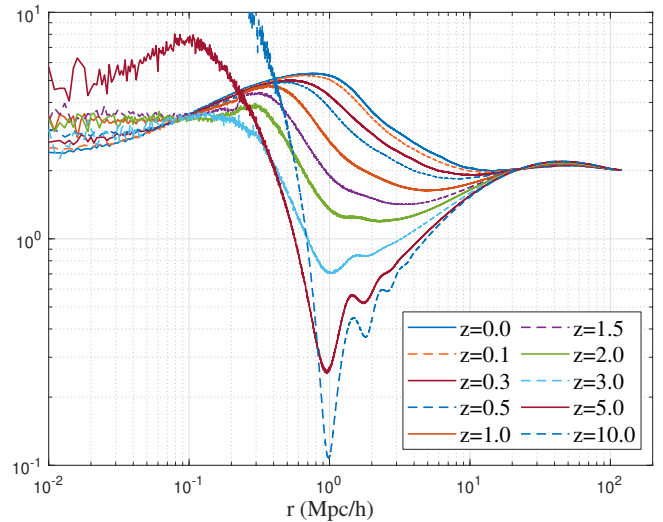


**Figure 21.** The variation of pairwise velocity dispersion  $S_2^{lp}(r)/u^2$  with scale  $r$  and redshifts  $z$ . The two limits  $S_2^{lp}(r \rightarrow 0) = S_2^{lp}(r \rightarrow \infty) = 2u^2$  due to correlation coefficients  $\rho_L = 1/2$  and  $\rho_L = 0$  between longitudinal velocities  $u_L$  and  $u'_L$  on small and large scales. Two second order structure functions  $S_2^{lp}(r) \approx S_2^l(r)$  at high redshift  $z$  when velocity is still Gaussian and small scale structures are not fully developed.

and a modified version of longitudinal structure function  $S_2^l(r)$

$$S_2^l(r) = 2 \left( u^2 - L_2(r) \right). \quad (55)$$

With equations for  $\langle u_L^2 \rangle$  (see Xu 2022e, Eq. (136)) and longitudinal correlation function  $L_2 = \langle u_L u'_L \rangle$  (see Xu 2022e, Eq. (111)),  $S_2^{lp}(r)$  on large scale can be easily calculated. The structure function  $S_2^l(r)$  on small scale is also identified to follow a one-fourth law  $\propto r^{1/4}$  (see Xu 2022e, Eq. (137)). However, the knowledge of structure function  $S_2^{lp}(r)$  on small scale is still missing. Figure 21 presents the variation of pairwise velocity dispersion  $S_2^{lp}(r)$  with scale  $r$  and redshift  $z$  with limits  $S_2^{lp}(r \rightarrow 0) = S_2^{lp}(r \rightarrow \infty) = 2u^2$  due to correlation coefficient  $\rho_L = 1/2$  and  $\rho_L = 0$  on small and large scales. Also,  $S_2^{lp}(r) \approx S_2^l(r)$  for high redshift  $z$ , when velocity distribution is nearly Gaussian and  $\langle u_L^2 \rangle \approx u^2$  on all scales (Eqs. (54) and (55)).

Both two-thirds and four-fifths laws (Eq. (1)) in incompressible hydrodynamics are no longer valid for SG-CFD due to the collisionless nature of flow. However, since the peculiar velocity field is of constant divergence on small scale, second order structure and correlation functions for peculiar velocity should satisfy the same kinematic relations as if the peculiar velocity field is incompressible (Xu 2022e). In addition, just like the direct energy cascade in 3D incompressible turbulence, there also exists a constant energy flux  $\varepsilon_u < 0$  in the mass propagation range for inverse kinetic energy cascade from small to large mass scales (see Xu 2021f, Eqs. (27) and (48)) in SG-CFD. Therefore, we expect the second order structure function  $S_2^{lp}(r)$  on the small scale should be determined by the constant energy flux  $\varepsilon_u$  in some way.

Since the viscous effect is not present in SG-CFD, a reduced structure function  $S_{2r}^{lp} = S_2^{lp} - 2u^2$  can be introduced with a limit  $\lim_{r \rightarrow 0} S_{2r}^{lp} = 0$ . The limiting pairwise velocity dispersion is inherent to all particle pairs with  $r \rightarrow 0$  and equals the kinetic energy on small



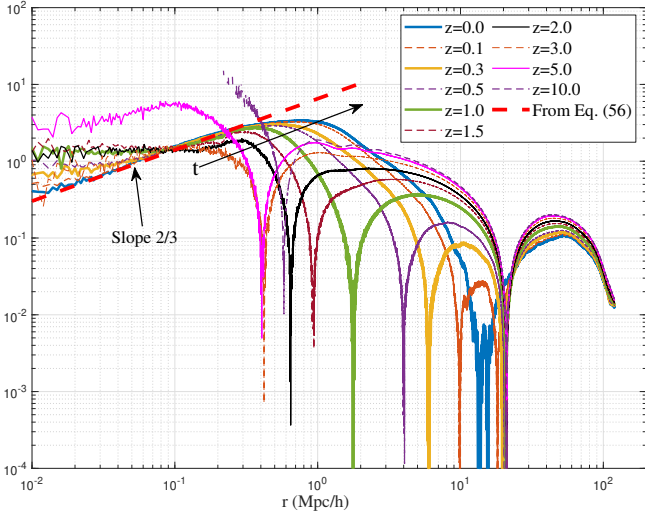


**Figure 22.** The variation of reduced longitudinal structure functions  $S_{2r}^{lp} = (S_2^{lp} - 2u^2)$  with scale  $r$  at different redshifts  $z$ , normalized by velocity dispersion  $u^2(a)$ . A scaling of  $S_{2r}^{lp} \propto (-\varepsilon_u)^{2/3} r^{2/3}$  (two-thirds law) can be clearly identified in a range that is gradually expanding with time, where  $\varepsilon_u < 0$  is the constant rate of energy cascade. The model from Eq. (56) is also presented for comparison. This relation might be used to predict dark matter particle mass and properties on small scale (Xu 2022i).

scale,  $\lim_{r \rightarrow 0} S_{2r}^{lp} = \lim_{r \rightarrow 0} \langle u_L^2 \rangle = 2u^2$ . The reduced structure function  $S_{2r}^{lp}$  is the extra pairwise velocity dispersion purely due to the inverse energy cascade. It should be determined by and only by the constant energy flux  $\varepsilon_u$  ( $m^2/s^3$ ) and scale  $r$ . By a simple dimensional analysis,  $S_{2r}^{lp}$  must follow a two-thirds law, i.e.  $S_{2r}^{lp} \propto (-\varepsilon_u)^{2/3} r^{2/3}$ .

Here to test this idea, Figure 22 plots the variation of reduced second order structure function  $S_{2r}^{lp}$  with scale  $r$  at different redshifts  $z$ . The range with  $S_{2r}^{lp} \propto r^{2/3}$  can be clearly identified that is formed along with the formation of halo structures. This range gradually extends to smaller and smaller length scales with time. This is a very interesting finding that the constant energy flux  $\varepsilon_u$  determines a new two-thirds law for a reduced second order structure function  $S_{2r}^{lp}$  in self-gravitating collisionless dark matter flow.

As expected, the reduced structure function quickly converges to  $S_{2r}^{lp} \propto (-\varepsilon_u)^{2/3} r^{2/3}$  with halo structures developed. The length scale at which  $S_{2r}^{lp}$  is at its maximum is about  $r_d \approx 0.7aMpc/h$ , same as the length scale for  $\langle u_L^2 \rangle$  (see Xu 2022e, Fig. 22). Therefore, second order longitudinal structure function (pairwise velocity dispersion) on small scale can be finally modelled as,

$$S_{2r}^{lp}(r) = u^2 \left[ 2 + \beta_2^* \left( \frac{r}{r_s} \right)^{2/3} \right] = 2u^2 + a^{3/2} \beta_2^* (-\varepsilon_u)^{2/3} r^{2/3}, \quad (56)$$

where the length scale  $r_s$  is purely determined by  $u_0$  and  $\varepsilon_u$  with

$$r_s = -\frac{u_0^3}{\varepsilon_u} = \frac{4}{9} \frac{u_0}{H_0} = \frac{2}{3} u_0 t_0 \approx 1.58 Mpc/h, \quad (57)$$

which is roughly the scale below which two-thirds law is valid. Rate of energy cascade  $\varepsilon_u$  is estimated as,

$$-\varepsilon_u = \frac{3}{2} \frac{u_0^2}{t_0} = \frac{9}{4} u_0^2 H_0 \approx 0.6345 \frac{u_0^3}{Mpc/h} = 4.6 \times 10^{-7} m^2/s^3. \quad (58)$$

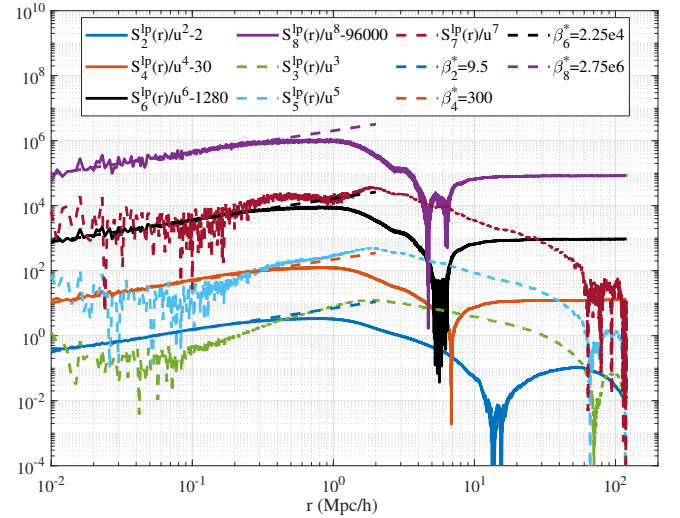


**Figure 23.** The variation of even and odd order structure functions with scale  $r$  at  $z=0$ . The plot demonstrates that even order reduced structure functions scales as  $S_{2nr}^{lp} \propto \beta_{2n}^* r^{2/3}$  on small scale (Eq. (61)), while odd order structure functions scales as  $S_{2n+1}^{lp} \propto r$ . The numbers 2, 30, 1280... are related to the generalized kurtosis  $K_{2n}(\Delta u_L, r)$  for the limiting distribution of pairwise velocity  $\Delta u_L$  when  $r \rightarrow 0$  (Eq. (61)).

Constant  $\beta_2^* \approx 9.5$  can be found from Fig. 22, where the model (56) is also presented for comparison.

With the model for  $S_{2r}^{lp}(r)$  in Eq. (56), Eq. (54), and model for longitudinal correlation  $L_2(r)$  (see Xu 2022e, Eq. (138)),

$$L_2(r) = u^2 \left[ 1 - \left( \frac{r}{r_1} \right)^n \right], \quad (59)$$

the dispersion  $\langle u_L^2 \rangle$  of longitudinal velocity (in Fig. 20) on small scale can be finally modeled as,

$$\langle u_L^2 \rangle = u^2 \left[ 2 - \left( \frac{r}{r_1} \right)^n + \frac{1}{2} \beta_2^* \left( \frac{r}{r_s} \right)^{2/3} \right], \quad (60)$$

where  $n \approx 1/4$  and  $r_1(a) \approx 19.4a^{-3} Mpc/h$ .

Next, the higher order structure functions can be similarly studied. Figure 23 plots the variation of even and odd order structure functions  $S_{2n+1}^{lp}(r)$  with scale  $r$  at  $z=0$ . It is now clear that the original Kolomgrov's scaling (Eq. (1)) for incompressible flow does not apply for self-gravitating collisionless dark matter flow. On small scale, all even order reduced structure functions follow the same scaling of  $S_{2nr}^{lp} \propto \beta_{2n}^* r^{2/3}$ , while all odd order structure functions follow a linear scaling such that  $S_{2n+1}^{lp} \propto r$ .

The general form for even order structure function  $S_{2n}^{lp}(r)$  can be precisely modeled as,

$$S_{2n}^{lp}(r) = u^{2n} \left[ 2^n K_{2n}(\Delta u_L, 0) + \beta_{2n}^* \left( \frac{r}{r_s} \right)^{2/3} \right], \quad (61)$$

where  $K_{2n}(\Delta u_L, r=0)$  is the generalized kurtosis on the smallest scale that we can find from Fig. 15 (given in Table 4 and modeled by Eq. (80)). The universal constants  $\beta_{2n}^*$  are determined as

$$\beta_2^* = 9.5, \beta_4^* = 300, \beta_6^* = 2.25 \times 10^4, \quad \text{and} \quad \beta_8^* = 2.75 \times 10^6 \quad (62)$$

or approximately

$$\beta_{2n}^* \approx 10^{1.826n-1.003}.$$

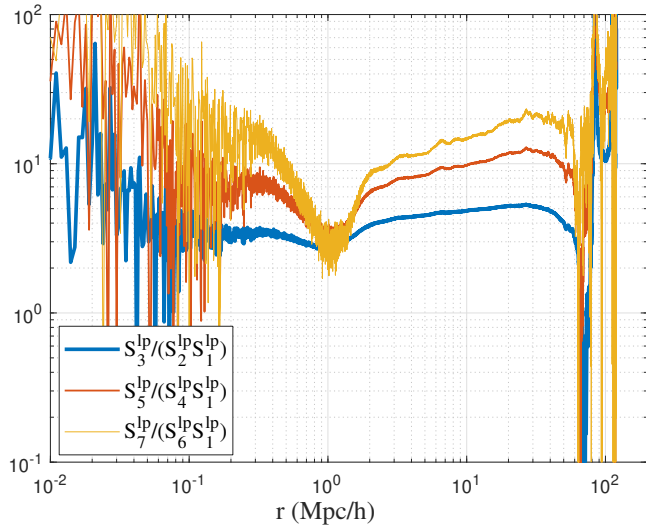


**Figure 24.** The variation of ratio  $S_{2n+1}^{lp}(r)/[S_1^{lp}(r)S_{2n}^{lp}(r)]$  for  $n = 1, 2,$  and  $3$  with scale  $r$  at  $z=0$ . For  $n=1$ , this ratio is around  $3$  as predicted by the generalized stable clustering hypothesis (GSCH) (Xu 2021d).

#### 4.6 GSCH for odd order moments of pairwise velocity

The mean pairwise velocity (first moment)  $S_1^{lp}(r) = -Har$  on small scale (Fig. 18) is from the stable clustering hypothesis, which can be precisely demonstrated by a two-body collapse model (TBCM) in expanding background (see Xu 2021d, Eq. (117)). The same TBCM model can be extended to higher order moments, i.e. the generalized stable clustering hypothesis (see Xu 2021d, Eq. (123)),

$$S_{2n+1}^{lp}(r) = (2n+1) S_1^{lp}(r) S_{2n}^{lp}(r), \quad (63)$$

or equivalently

$$S_{2n+1}^{lp}(r) = -2^n (2n+1) K_{2n}(\Delta u_L, r=0) Haru^{2n}. \quad (64)$$

The generalized kurtosis on the smallest scale  $K_{2n}(\Delta u_L, r=0)$  is presented in next section (Table 4 and Eq. (80)). With odd moments from Fig. 23, Fig. 24 presents the ratio  $S_{2n+1}^{lp}(r)/[S_1^{lp}(r)S_{2n}^{lp}(r)]$  for  $n=1, 2$  and  $3$  at  $z=0$ . For  $n=1$ , this ratio is around  $3$  on small scale. For  $n=2$  and  $3$ , this ratio slightly deviates from predicted value of  $(2n+1)$  with greater noise on small scale (see Xu 2021d, Fig. 8).

Finally, Table 3 presents a complete comparison of velocity field between incompressible hydrodynamics and self-gravitating collisionless dark matter flow (SG-CFD).

## 5 REDSHIFT AND SCALE VARIATION OF VELOCITY DISTRIBUTIONS

### 5.1 Modeling velocity distributions on small scale

On small scale, velocities  $u_L$  and  $\Sigma u_L$  should have the same limiting distribution with  $r \rightarrow 0$  (Fig. 15). Velocity distribution that maximizes the system entropy was studied in our previous work (see Xu 2021c, Fig. 4). Based on the halo description of self-gravitating system,  $u_L$  on small scale should follow a  $X$  distribution to maximize system entropy. The  $X$  distribution reads (see Xu 2021c, Eq. (32)),

$$X(v) = \frac{1}{2\alpha v_0} \frac{e^{-\sqrt{a^2+(v/v_0)^2}}}{K_1(\alpha)}, \quad (65)$$

**Table 3.** The velocity fields of incompressible flow and SG-CFD

Quantity	Incompressible flow	Self-gravitating collisionless flow
$\langle u_L \rangle$	0 for all scale $r$	$\lim_{r \rightarrow 0, \infty} \langle u_L \rangle = 0$ varying with $r$
$\langle u_L^2 \rangle$	$u^2$ for all scale $r$	$\lim_{r \rightarrow 0} \langle u_L^2 \rangle = 2u^2$ $\lim_{r \rightarrow \infty} \langle u_L^2 \rangle = u^2$
$\langle u_L^3 \rangle$	0 for all scale $r$	$\lim_{r \rightarrow 0, \infty} \langle u_L^3 \rangle = 0$ varying with $r$
PDF of $u_L$	Gaussian	Non-gaussian on all scales
$\langle \Delta u_L \rangle$	0 for all scale $r$	$\lim_{r \rightarrow 0, \infty} \langle \Delta u_L \rangle = 0$ varying with $r$
$\langle \Delta u_L^2 \rangle$	$\lim_{r \rightarrow 0} \langle \Delta u_L^2 \rangle = 0$ $\lim_{r \rightarrow \infty} \langle \Delta u_L^2 \rangle = u^2$	$\lim_{r \rightarrow 0} \langle \Delta u_L^2 \rangle = 2u^2$ $\lim_{r \rightarrow \infty} \langle \Delta u_L^2 \rangle = 2u^2$
$K_3(\Delta u_L)$	$\lim_{r \rightarrow 0} K_3(\Delta u_L) = -0.4$ $\lim_{r \rightarrow \infty} K_3(\Delta u_L) = 0$	$\lim_{r \rightarrow 0, \infty} K_3(\Delta u_L) = 0$ varying with $r$
$K_4(\Delta u_L)$	$\lim_{r \rightarrow 0} K_4(\Delta u_L) \approx 4$ (depends on Re) $\lim_{r \rightarrow \infty} K_4(\Delta u_L) = 3$ (Gaussian)	$\lim_{r \rightarrow 0} K_4(\Delta u_L) = 7.5$ $\lim_{r \rightarrow \infty} K_4(\Delta u_L) = 4.2$
$\langle \Sigma u_L \rangle$	0 on all scales	0 on all scales
$\langle \Sigma u_L^2 \rangle$	$\lim_{r \rightarrow 0} \langle \Sigma u_L^2 \rangle = 4u^2$ $\lim_{r \rightarrow \infty} \langle \Sigma u_L^2 \rangle = 2u^2$	$\lim_{r \rightarrow 0} \langle \Delta u_L^2 \rangle = 6u^2$ $\lim_{r \rightarrow \infty} \langle \Delta u_L^2 \rangle = 2u^2$

where  $\alpha$  is a shape parameter and  $K_n(x)$  is the *modified* Bessel function of the second kind. The velocity scale  $v_0$  satisfies

$$\alpha \frac{K_2(\alpha)}{K_1(\alpha)} v_0^2 = \langle u_L^2 \rangle, \quad (66)$$

where  $\langle u_L^2 \rangle$  is the dispersion of velocity  $u_L$  in Fig. 19. It can be estimated that  $v_0^2 \approx 0.84u_0^2$  with  $\langle u_L^2 \rangle(r=0.1Mpc/h) = 2.5u_0^2$  (from Fig. 19) at  $z=0$ . With shape parameter  $\alpha \approx 1.33$  and  $v_0^2 = 0.84u_0^2$ , the  $X$  distribution is plotted in Fig. 25 for comparison with the distribution of velocity  $u_L$ . The velocity sum  $\Sigma u_L$  should also follow the same  $X$  distribution with a different variance, i.e.  $\langle (\Sigma u_L)^2 \rangle \approx 3\langle u_L^2 \rangle$ . All distributions are symmetric on small scale.

The longitudinal velocity has a finite limiting correlation  $\rho_L = 1/2$  at  $r=0$  (see Xu 2022e, Fig. 16) such that the limiting distribution of velocity difference (pairwise velocity)  $\Delta u_L$  must be different from the distribution of  $u_L$  (different Kurtosis in Fig. 15). This effect, i.e. the correlation between longitudinal velocities  $u_L$  and  $u'_L$  from the same halo decreases with increasing halo size (Eq. (73)) (also see Xu 2022e, Section 3.3.1), was not considered in previous work to find the distribution of  $\Delta u_L$  (Sheth 1996). The distribution of  $\Delta u_L$  on small scale cannot be Gaussian because of strong gravitational interaction (also see Fig. 15), whose moment and kurtosis can be estimated in next Section.

### 5.2 Distribution of pairwise velocity on small scale

The limiting distribution of  $\Delta u_L$  when  $r \rightarrow 0$  is different from the distribution of  $u_L$  (Figs. 15 and 25). The explicit form of that distribution is still unknown and should be explored in the future. However, the moments of  $\Delta u_L$  when  $r \rightarrow 0$  can be rigorously estimated. This is required to compute the generalized kurtosis in Eq. (61) for modeling pairwise velocity on small scale.

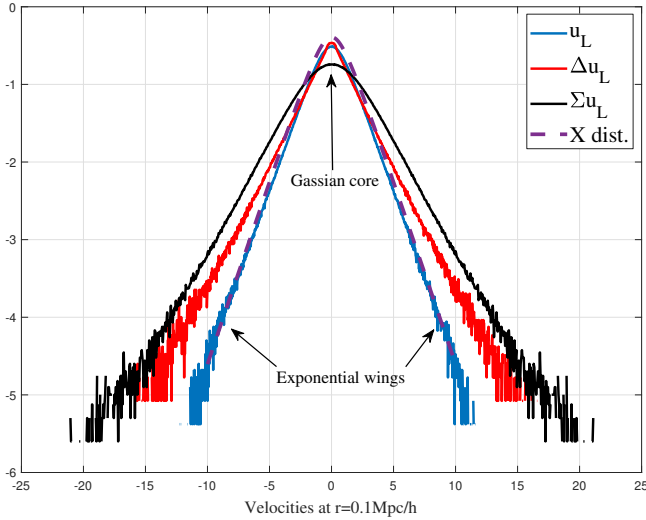


**Figure 25.** Distributions of  $u_L$ ,  $\Delta u_L$ , and  $\Sigma u_L$  on scale of  $r=0.1\text{Mpc/h}$  at  $z=0$ , i.e.  $\log_{10} P_{uL}$  vs.  $u_L/u_0$ . All distributions are symmetric with a vanishing skewness. The  $X$  distribution that maximizes the system entropy (Eq. (65)) is also plotted and matches the distribution of longitudinal velocity  $u_L$ . Distributions have a Gaussian core for small velocity and exponential wings for large velocity.

Let's start from the  $H$  distribution for the fraction of particles with a velocity dispersion  $\sigma_v^2$  (i.e. the virial dispersion of a halo that particle belongs to) (see Xu 2021c,e, Eq. (6)). For system with total  $N$  collisionless particles, total number of particles in a halo group with all halos of the same size  $n_p$  should be

$$n_p N_h = NH(\sigma_v^2) d\sigma_v^2, \quad (67)$$

where  $N_h$  is the number of halos in a halo group of size  $n_p$ .

Let's assume the number of particle pairs  $n_{pair}$  with a small separation  $r$  from halos of size  $n_p$  is proportional to the halo size  $n_p$  with a power law,  $n_{pair} = \mu_p (n_p)^{\alpha_p}$ , where  $\mu_p$  is a proportional constant. The maximum number of pairs for a given halo size  $n_p$  is  $n_{pair} = n_p (n_p - 1) / 2$  if all  $n_p$  particles in that halo collapse to a single point, where we should have  $\alpha_p = 2$ . In reality, the exponent  $\alpha_p$  should satisfy  $1 < \alpha_p < 2$ .

The number of pairs in a halo group ( $N_h$  halos of size  $n_p$ ) reads,

$$N_h n_{pair} = N \mu_p (n_p)^{\alpha_p - 1} H(\sigma_v^2) d\sigma_v^2,$$

or the total number of pairs with a given separation  $r$  in entire  $N$ -body system should be,

$$N_{pair} = \int_0^\infty N \mu_p (n_p)^{\alpha_p - 1} H(\sigma_v^2) d\sigma_v^2. \quad (68)$$

From virial theorem, the halo size  $\sigma_v^2 \propto (n_p)^{2/3}$  and we can write  $n_p = \mu_v (\sigma_v^2 / \sigma_h^2)^{3/2}$ , where  $\sigma_h^2$  is the halo velocity dispersion (the dispersion of halo velocity in a halo group) that is independent of halo mass (see Xu 2021f, Fig. 2) and  $\mu_v$  is a proportional constant.

The  $H$  distribution is naturally related to the dimensionless halo mass function  $f(v)$  (see Xu 2021e, Eq. (59)),

$$H(\sigma_v^2) d\sigma_v^2 = f(v) dv, \quad (69)$$

where the dimensionless variable  $v = \sigma_v^2 / \sigma_h^2$ . Therefore, Eq. (68)

can be transformed to

$$\frac{N_{pair}}{N \mu_p (\mu_v)^{\alpha_p - 1}} = \int_0^\infty f(v) v^{\frac{3}{2}(\alpha_p - 1)} dv$$

or equivalently, (70)

$$\int_0^\infty \beta_p f(v) v^p dv = 1,$$

i.e.  $\beta_p f(v) v^p dv$  is the fraction of pairs in halo group with a given size where the exponent

$$p = 3(\alpha_p - 1) / 2. \quad (71)$$

Since velocity  $u_L$  from the same halo group is nearly Gaussian (see Xu 2021c, Fig. 3), the distribution of  $\Delta u_L = u'_L - u_L$  can be obtained from the joint Gaussian distribution of  $u_L$  and  $u'_L$  with a halo size-dependent correlation coefficient  $\rho_{cor}(n_p)$ ,

$$P_{\Delta u_L}(x) = \int_0^\infty \frac{e^{-x^2/[4(1-\rho_{cor})\sigma^2]} \beta_p f(v) v^p dv}{\sqrt{2\pi} \sqrt{2(1-\rho_{cor})} \sigma}. \quad (72)$$

The correlation  $\rho_{cor}$  (see Xu 2022e, Eq. (58)) and the total particle velocity dispersion  $\sigma^2$  read

$$\rho_{cor}(n_p) = \sigma_h^2 / \sigma^2 \quad \text{and} \quad \sigma^2(n_p) = \sigma_v^2(n_p) + \sigma_h^2, \quad (73)$$

where  $\sigma_h^2$  and  $\sigma_v^2$  are the halo velocity dispersion and halo virial dispersion, respectively.

The moment generating function and the corresponding moments can be finally obtained from Eq. (72),

$$\begin{aligned} \int_{-\infty}^\infty P_{\Delta u_L}(x) e^{xt} dx &= \int_0^\infty \beta_p f(v) v^p e^{(1-\rho_{cor})\sigma^2 t^2} dv \\ &= \int_0^\infty \beta_p f(v) v^p e^{v \sigma_h^2 t^2} dv, \end{aligned} \quad (74)$$

$$M_m(\Delta u_L) = \frac{m!}{(m/2)!} \int_0^\infty \beta_p f(v) v^{p+m/2} dv \sigma_h^m. \quad (75)$$

We can use the double- $\lambda$  mass function (see Xu 2021a, Eq. (98)) that is proposed based on the inverse mass cascade theory, where the dimensionless mass function  $f(v)$  reads,

$$f(v) = f_{D\lambda}(v) = \frac{(2\sqrt{\eta_0})^{-q}}{\Gamma(q/2)} v^{q/2-1} \exp\left(-\frac{v}{4\eta_0}\right), \quad (76)$$

where  $\eta_0 = 0.76$  and  $q = 0.556$  for the best fit of mass function to simulation data. The normalization factor in Eq. (70) should be

$$\beta_p = \frac{N \mu_p (\mu_v)^{\alpha_p - 1}}{N_{pair}} = \frac{\Gamma(q/2)}{(2\sqrt{\eta_0})^{2p} \Gamma(p+q/2)}. \quad (77)$$

Finally, the distribution of pairwise velocity  $P_{\Delta u_L}$  should satisfy (from Eq. (74))

$$\int_{-\infty}^\infty P_{\Delta u_L}(x) e^{xt} dx = \frac{1}{(1 - 4\eta_0 \sigma_h^2 t^2)^{p+q/2}}, \quad (78)$$

such that the moments of any order  $m$  can be obtained as,

$$M_m(\Delta u_L) = \frac{m! (2\sqrt{\eta_0})^m}{(m/2)! \Gamma(p+q/2)} \Gamma\left(\frac{1}{2}(m+2p+q)\right) \sigma_h^m. \quad (79)$$

The generalized kurtosis for pairwise velocity  $\Delta u_L$  on small scale is,

$$K_{2n}(\Delta u_L) = \frac{(2n)! \Gamma(n+p+q/2) [\Gamma(p+q/2)]^{n-1}}{n! 2^n [\Gamma(1+p+q/2)]^n}. \quad (80)$$

**Table 4.** Generalized kurtosis of velocity on small and large scales at  $z=0$ 

Scale	Velocity fields	Distribution	$4^{th}$	$6^{th}$	$8^{th}$
$r \rightarrow 0$	$u_L, \Sigma u_L$	N-body, $z=0$ , Fig. 15	4.8	57	1200
$r \rightarrow 0$	$\Delta u_L$	N-body, $z=0$ , Fig. 15	7.5	160	6000
$r \rightarrow 0$	$u_L, \Sigma u_L$	$X(x)$ (Eq. (65))	4.6	48.9	944.8
$r \rightarrow 0$	$\Delta u_L$	Eq. (80)	7.7	159.24	6356
$r \rightarrow \infty$	$\Delta u_L, \Sigma u_L$	N-body, $z=0$ , Fig. 15	<b>4.181</b>	<b>41.46</b>	<b>670.8</b>
$r \rightarrow \infty$	$u_L$	N-body, $z=0$ Fig. 15	5.39	85.78	2800
$r \rightarrow \infty$	$\Delta u_L, \Sigma u_L$	Logistic (Eq. (82))	4.2	279/7	685.8
$r \rightarrow \infty$	$u_L$	$P_{uL}(x)$ (Eq. (85))	5.4	78.4	2269.8
		Laplace distribution	6	90	2520
		Gaussian distribution	<b>3</b>	<b>15</b>	<b>105</b>

With  $\eta_0 = 0.76$  and  $q = 0.556$  for double- $\lambda$  mass function (see Xu 2021a, Eq. (98)),  $\beta_p \approx 1.5426$  from Eq. (77). Using the Kurtosis values for  $\Delta u_L$  on small scale from simulation (Table 4), the parameter  $p \approx 0.36$  or exponent  $\alpha_p \approx 1.24$  (from Eq. (71)) can be obtained, and the total number of pairs  $N_{pair}$  with  $r \rightarrow 0$  should be (from Eq. (77))

$$\frac{N_{pair}}{N} = \frac{\mu_p (\mu_v)^{\alpha_p - 1}}{\beta_p}, \quad (81)$$

where both constants  $\mu_p$  and  $\mu_v$  can be obtained from simulation ( $\mu_p \approx 0.21$  and  $\mu_v \approx 14$  from N-body simulation in Section 2 for particle pairs with a separation of  $r=0.1\text{Mpc/h}$ ).

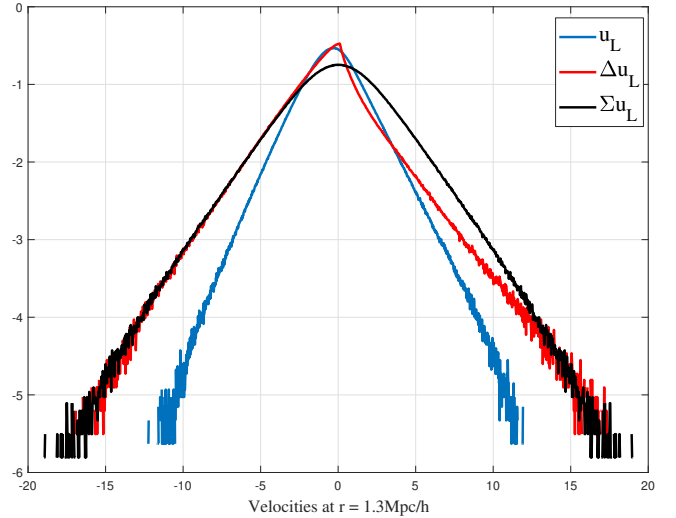
The general kurtosis for  $\Delta u_L$  computed from Eq. (80) are listed in Table 4 and agrees well with N-body simulation. Table 4 lists the generalized kurtosis of three types of velocities on small and large scales, both from simulations and corresponding models.

Again, the pairwise velocity  $\Delta u_L$  is usually approximated by an exponential (Laplace) distribution (Sheth 1996). This seems not accurate as the generalized kurtosis of distribution of  $\Delta u_L$  from N-body simulations does not agree with that of exponential distribution on both small and large scales.

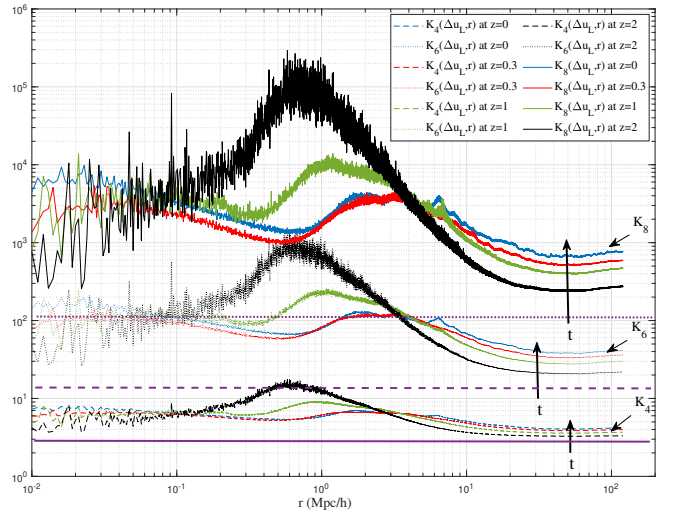
### 5.3 Velocity distributions on intermediate scale

Figure 26 presents velocity distributions on the intermediate scale  $r_r=1.3\text{Mpc/h}$ . Distributions of  $\Delta u_L$  and  $u_L$  are non-symmetric with nonzero skewness that is necessary as kinetic energy cascaded from small scale needs to be consumed to grow halos on the intermediate scale. The velocity sum  $\Sigma u_L$  is symmetric on all scales.

Figure 27 plots the redshift variation of generalized kurtosis  $K_4$ ,  $K_6$  and  $K_8$  of pairwise velocity  $\Delta u_L$  for  $z=0, 0.3, 1$ , and  $2.0$ . Kurtosis of Gaussian distribution is also plotted for reference. All velocities are initially Gaussian. With most pairs of particles from the same halo, the distribution of pairwise velocity  $\Delta u_L$  on small scale converges to limiting distribution (Eq. (80)) much faster due to strong intra-halo gravitational interaction. While the distribution of  $\Delta u_L$  for particle pairs from different halos on large scale converges much slower due to weaker inter-halo gravitational interaction and greater distance. We will revisit this in Fig. 30. Kurtosis on the intermediate scales is much greater than that on both small and large scales. Figure 28 plots the variation of  $K_3$  (or skewness) of pairwise velocity  $\Delta u_L$  for  $z=0, 0.3, 1$ , and  $2.0$  on small and intermediate scales. The skewness  $K_3 \approx 0$  on small scale and  $K_3 < 0$  on intermediate scale. A non-zero skewness is a necessary feature of inverse energy cascade.



**Figure 26.** Distributions of  $u_L$ ,  $\Delta u_L$ , and  $\Sigma u_L$  on intermediate scale of  $r = 1.3$  Mpc/h at  $z=0$ , i.e.  $\log_{10} P_{uL}$  vs.  $u_L/u_0$ . Distribution of  $\Sigma u_L$  is symmetric, while the distribution of  $\Delta u_L$  is non-symmetric with non-zero (negative) skewness (Fig. 28) and skew toward positive side. This is a necessary feature of inverse energy cascade. The distribution of  $u_L$  is also non-symmetric with a non-zero mean  $\langle u_L \rangle$ .



**Figure 27.** The redshift evolution of generalized kurtosis for pairwise velocity  $\Delta u_L$  at redshift  $z= 2.0, 1.0, 0.3$ , and  $0$ . Kurtosis for Gaussian distribution are also plotted for reference (purple lines). The distribution of  $\Delta u_L$  is non-Gaussian on all scales, while the evolution of distribution is much faster on small scale due to strong gravitational interaction in halos (also see Fig. 30).

### 5.4 Modeling velocity distributions on large scale

On large scale, velocities  $\Delta u_L$  and  $\Sigma u_L$  have the same distribution with  $r \rightarrow \infty$  (Fig. 15 and Table 4). The distribution of  $u_L$  at  $r \rightarrow \infty$  has greater kurtosis than  $\Delta u_L$  and  $\Sigma u_L$ . The non-Gaussian feature on large scale could be a manifestation of the long-range nature of gravitational interaction. By contrast, velocity is always Gaussian on large scale for incompressible flow with short range interaction.

The distribution of pairwise velocity  $\Delta u_L$  on large scale is usually assumed to be exponential in literature that is not smooth (non-



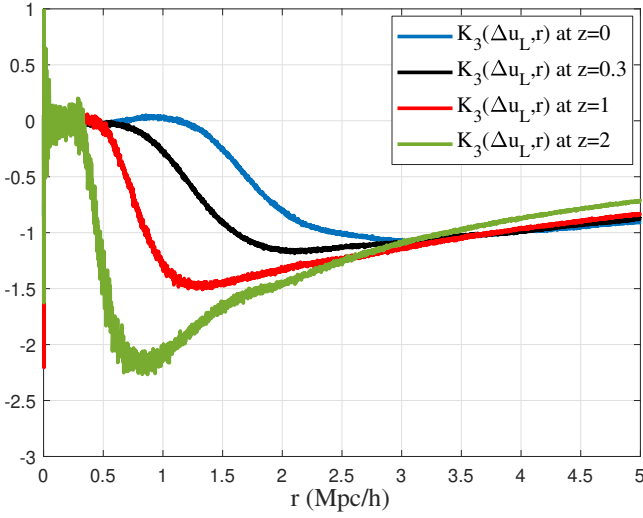


**Figure 28.** The redshift evolution of skewness  $K_3$  (third order generalized kurtosis) of  $\Delta u_L$  on intermediate scale. The skewness  $K_3 \approx 0$  on small scale and  $K_3 < 0$  on intermediate scale. A non-zero skewness is a necessary feature of inverse energy cascade.

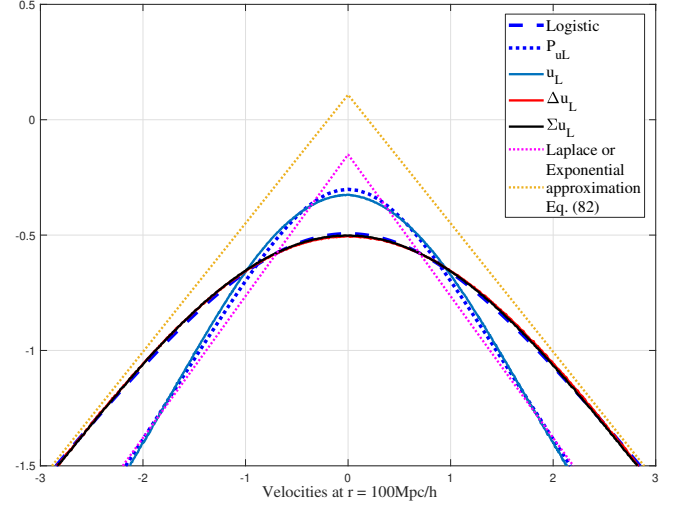


**Figure 29b.** Comparison of proposed distributions with simulation data for small velocities. Logistic distribution for  $\Delta u_L$  shows better agreement for small velocities than exponential approximation.

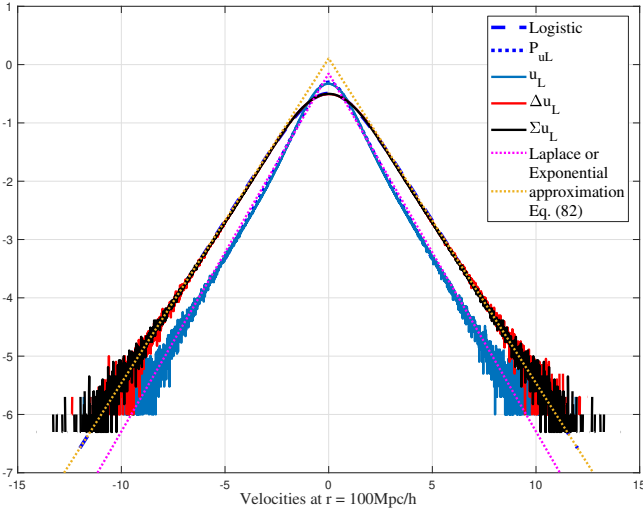


**Figure 29a.** Distributions of  $u_L$ ,  $\Delta u_L$ , and  $\Sigma u_L$  on scale of  $r = 100$  Mpc/h at  $z=0$ , i.e.  $\log_{10} P_{u_L}$  vs.  $u_L/u_0$  (normalized by  $u_0$ ). On large scale, all distributions are symmetric. A logistic distribution can be used to model the distribution of  $\Delta u_L$  and  $\Sigma u_L$ . At large velocity, all distributions approach an exponential function.

differentiable) at zero velocity (Fig. 29a and 29b). An improvement can be a Logistic distribution for both  $\Delta u_L$  and  $\Sigma u_L$  with a variance of  $(\pi s)^2/3 = 2u^2$ , where  $u^2$  is the one dimensional velocity dispersion of the entire N-body system (or the variance of  $u_L$  on large scale),

$$P_{\Delta u_L}(x) = \frac{1}{4s} \sec^2 \left( \frac{x}{2s} \right).$$

For large  $x$ , the logistic distribution will reduce to an exponential distribution,

$$P_{\Delta u_L}(x \rightarrow \infty) \approx \frac{1}{s} \exp\left(-\frac{x}{s}\right). \quad (82)$$

Let's assume  $P_{u_L}$  being the limiting distribution of  $u_L$  when  $r \rightarrow$

$\infty$ . With  $\rho_L = 0$  at  $r \rightarrow \infty$ , two distributions should satisfy the convolution

$$P_{\Delta u_L}(z) = \int_{-\infty}^{\infty} P_{u_L}(x) P_{u_L}(z-x) dx. \quad (83)$$

Using the characteristic function, the Fourier transform of two distributions should satisfy,

$$\hat{P}_{\Delta u_L}(t) = [\hat{P}_{u_L}(t)]^2 = \frac{\pi s t}{\sinh(\pi s t)}. \quad (84)$$

The moment-generating function of  $u_L$  can be found from Eq. (84) with a variance of  $(\pi s)^2/6 = u^2$ ,

$$MGF_{P_{u_L}}(t) = \sqrt{\frac{\pi s t}{\sin(\pi s t)}}. \quad (85)$$

The explicit form of distribution  $P_{u_L}(x)$  from Eq. (84) is not available but can be obtained numerically from Eq. (85), via inverse Fourier transform. All distributions (Eqs. (82) and (85)) are plotted in Fig. 29a and compared against simulation data with good agreement. All distributions are approximately exponential at large velocity. On large scale, pair of particles are not likely residing in the same halo. With pair of particles from different halos, velocity on large scale should reflect the velocity of halos that particles reside in. Kurtosis of velocity distributions on large scale is presented in Table 4.

## 5.5 Redshift evolution of velocity distributions

Finally, the redshift evolution of distributions of all different types of velocities is summarized in this section. This includes velocity  $u_p$  of all particles, velocity  $u_{hp}$  of all halo particles, velocity  $u_{op}$  of all out-of-halo particles, velocity  $u_h$  of all halos, and three longitudinal velocities  $u_L$ ,  $\Delta u_L$ , and  $\Sigma u_L$  on small and large scales, respectively.

If any velocity always follows a family of  $X$  distribution with a time-varying shape parameter  $\alpha$  (Eq. (65)), the redshift evolution of that velocity distribution can be reduced to the redshift dependence of shape parameter  $\alpha \equiv \alpha(z)$ . Therefore, the redshift evolution of velocity distributions can be presented as the variation of generalized kurtosis that is a function of  $\alpha(z)$ . The  $m$ th order generalized kurtosis

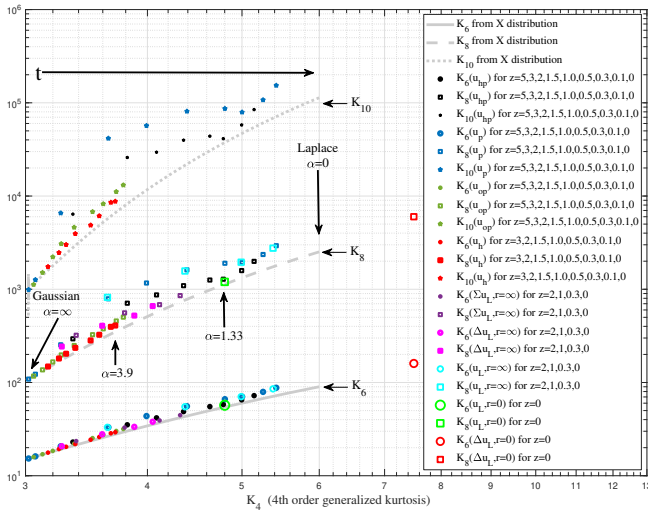


**Figure 30.** The redshift evolution of generalized kurtosis  $K_6$ ,  $K_8$ , and  $K_{10}$  with  $K_4$  for different types of velocities, i.e. velocity  $u_p$  of all particles in system, velocity  $u_{hp}$  of all halo particles, velocity  $u_{op}$  of all out-of-halo particles, velocity  $u_h$  of all halos, and longitudinal velocity  $u_L$ , pairwise velocity  $\Delta u_L$ , and velocity sum  $\Sigma u_L$  on small and large scales. All velocities are initially Gaussian with shape parameter  $\alpha = \infty$  for  $X$  distribution and gradually evolving toward non-Gaussian with a decreasing  $\alpha$  with time. The evolution (approximately) follows the prediction (gray lines) of  $X$  distribution. The distributions of out-of-halo particles  $u_{op}$  and halo velocity  $u_h$  matches each other and evolves at a much slower pace compared to halo particles  $u_p$ . Halos can be treated as macro-particle with similar velocity distribution as that of out-of-halo particles.

of  $X$  distribution can be found as (see Xu 2021c, Eq. (41)),

$$K_m(X) = \left( \frac{2K_1(\alpha)}{K_2(\alpha)} \right)^{m/2} \frac{\Gamma((1+m)/2)}{\sqrt{\pi}} \cdot \frac{K_{(1+m)/2}(\alpha)}{K_1(\alpha)}. \quad (86)$$

Figure 30 presents a summary of the redshift evolution of velocity distributions in terms of the generalized kurtosis of different order (4<sup>th</sup>, 6<sup>th</sup>, 8<sup>th</sup>, and 10<sup>th</sup> kurtosis from both simulation and Eq. (86)). With increasing time, all velocities become non-Gaussian and the evolution approximately follows the prediction of  $X$  distribution with a decreasing  $\alpha$ . In principle, the halo velocity ( $u_h$ ), out-of-halo particle velocity ( $u_{op}$ ), and the halo particle velocity ( $u_{hp}$ ) should all follow a  $X$  distribution to maximize system entropy, just like the longitudinal velocity on small scale (Eq. (65)). The distributions of halo velocity ( $u_h$ ) and out-of-halo particle velocity ( $u_{op}$ ) have similar distributions and evolve at a much slower pace than the distributions of halo particle velocity ( $u_{hp}$ ) because gravity is much stronger on small scale. This is also consistent with the finding that virial equilibrium is established much faster for particles in halos (due to stronger gravity) than for halos themselves (see Xu 2021f, Fig. 9).

## 6 CONCLUSIONS

By identifying all halos in entire N-body system and dividing all particles into halo particles and out-of-halo particles that do not belong to any halos, the redshift and scale dependence of density and velocity distributions for halo and out-of-halo particles are extensively investigated.

Instead of projecting particle field onto structured grid that usually involves information loss and unnecessary noise, Delaunay tessellation is used to reconstruct the co-moving density field and maximally

preserve information in N-body simulation. The particle over-density  $\delta$  evolves from an initial Gaussian to an asymmetric distribution with a long tail  $\propto \delta^{-3}$  (Fig. 1a). The log-density  $\eta$  evolves from Gaussian to a bimodal distribution at  $z=0$ , with two peaks corresponding to the high density for halo particles and low density for out-of-halo particles (Fig. 2). The log-density distribution of out-of-halo particles has a negative mean decreasing with time, while that of halo particles has an increasing mean, both due to the continuous mass transfer from out-of-halo to halos (Fig. 5).

Without projecting the density field onto grid, we first compute the radial distribution function  $g(r)$  for all scale  $r$  from N-body simulation. The second order density correlation  $\xi(r)$  can be obtained from  $g(r)$  (Eq. (9)) and plotted in Figs. 6, 8 and 9. The density correlation cannot be positive on all scales due to the normalization (Eq. (10)). The density spectrum  $E_\delta$  and fluctuation function  $\sigma_\delta^2$  can be obtained from  $\xi(r)$  using Eqs. (20) and (27), and presented in Figs. 6, 7, 11. Function  $E_{\delta r}$  reflects the real-space distribution of density fluctuation on different scales (Eq. (30) and Fig. 12) and contains the same information as density spectrum  $E_\delta$  (Eq. (31)). Analytical models for correlation and dispersion functions on large scale are also presented in Eqs. (33), (35), Figs. 6 and 11.

The scale dependence of velocity field is studied for the longitudinal velocity  $u_L$  or  $u'_L$ , velocity difference  $\Delta u_L = u'_L - u_L$  (or pairwise velocity), and velocity sum  $\Sigma u_L = u_L + u'_L$  (see Fig. 13). Fully developed velocity field is never Gaussian on any scale despite that they can be initially Gaussian (Figs. 14 and 15). By contrast, velocity distribution is nearly Gaussian on large scale for incompressible flow. Distribution of  $\Sigma u_L$  approaches that of  $u_L$  on small scale with the correlation (between  $u_L$  and  $u'_L$ )  $\rho_L \rightarrow 0.5$ . While on large scale, the distribution of  $\Sigma u_L$  approaches that of  $\Delta u_L$  with correlation  $\rho_L \rightarrow 0$ .

Combining pair conservation equation and density correlation, the first moment of  $\Delta u_L$  (pairwise velocity) can be analytically modelled on small and large scales (Eqs. (46), (48) and Fig. 18). The second moment of three types of velocities is presented in Figs. 19 and 20, with an initial increase with  $r$  followed by a sharp decrease on the intermediate scale.

The second moment of  $\Delta u_L$ , i.e. the pairwise velocity dispersion  $S_2^{lp}(r) = \langle (\Delta u_L)^2 \rangle$ , approaches  $2u^2$  on small scale (Fig. 21). A two-thirds law can be identified for a reduced structure function such that  $S_{2r}^{lp} = (S_2^{lp} - 2u^2) \propto (-\varepsilon_u)^{2/3} r^{2/3}$  (Eq. (56) and Fig. 22), where  $\varepsilon_u$  is the constant rate of energy cascade. A constant length scale can be introduced as  $r_s = u_0^3/\varepsilon_u$ , below which the two-thirds law is valid. Model for longitudinal velocity dispersion  $\langle u_L^2 \rangle$  on small scale can be derived (Eq. (60) and Fig. 19). The two-thirds law can be generalized to all even order structure functions  $\langle (\Delta u_L)^{2n} \rangle$  (Eq. (61) and Fig. 23), while odd order structure functions  $\langle (\Delta u_L)^{2n+1} \rangle \propto r$  should satisfy generalized stable clustering hypothesis (GSCH in Eq. (63) and Fig. 24). A complete comparison between incompressible flow and SG-CFD is listed in Table 3.

The distributions of three types of different velocities can be analytically modeled on small and large scales, respectively. On small scale, both velocities  $u_L$  and  $\Sigma u_L$  can be modelled by a  $X$  distribution to maximize system entropy (Fig. 25 and Eq. (65)). Explicit form for distribution of pairwise velocity  $\Delta u_L$  on small scale is still unknown. However, the moments and kurtosis of  $\Delta u_L$  can be analytically estimated (Eqs. (79) and (80)) using joint Gaussian distribution with a halo-size dependent correlation coefficient  $\rho_{cor}$  (Eq. (72)). On intermediate scale, distributions of  $u_L$  and  $\Delta u_L$  becomes significantly non-symmetric with non-zero skewness, a necessary feature of inverse energy cascade. On large scale, both  $\Delta u_L$  and  $\Sigma u_L$  approach

the same distribution and can be modelled by a logistic function (Eq. (82) and Fig. 29a). The distribution of  $u_L$  can also be analytically obtained in Eq. (84). The limiting distributions of different velocities on small and large scales are summarized in Table 4.

The redshift evolution of velocity distributions is summarized in Fig. 30. With increasing time, all velocities become non-Gaussian and the redshift evolution approximately follows the prediction of the  $X$  distribution with a decreasing  $\alpha(z)$  to continuously maximize system entropy. However, the distribution of velocities on large scale usually evolves at a much slower pace than the distribution of velocities on small scale because of stronger gravity on small scale.

## DATA AVAILABILITY

Two datasets underlying this article, i.e. a halo-based and correlation-based statistics of dark matter flow, are available on Zenodo (Xu 2022a,b), along with the accompanying presentation slides "A comparative study of dark matter flow & hydrodynamic turbulence and its applications" (Xu 2022c). All data files are also available on GitHub (Xu 2022d).

## REFERENCES

- Angulo R. E., Springel V., White S. D. M., Jenkins A., Baugh C. M., Frenk C. S., 2012, *Monthly Notices of the Royal Astronomical Society*, 426, 2046
- Batchelor G. K., 1953, *The Theory of Homogeneous Turbulence*. Cambridge University Press, Cambridge, UK
- Baugh C. M., Efstathiou G., 1994, *Monthly Notices of the Royal Astronomical Society*, 270, 183
- Baugh C. M., Gaztanaga E., Efstathiou G., 1995, *Monthly Notices of the Royal Astronomical Society*, 274, 1049
- Bernardeau F., Kofman L., 1995, *Astrophysical Journal*, 443, 479
- Bernardeau F., van de Weygaert R., 1996, *Monthly Notices of the Royal Astronomical Society*, 279, 693
- Colberg J. M., White S. D. M., Jenkins A., Pearce F. R., 1999, *Monthly Notices of the Royal Astronomical Society*, 308, 593
- Davis M., Peebles P. J. E., 1977, *Astrophysical Journal Supplement Series*, 34, 425
- Efstathiou G., Davis M., Frenk C. S., White S. D. M., 1985, *Astrophysical Journal Supplement Series*, 57, 241
- Ferreira P. G., Juszkiewicz R., Feldman H. A., Davis M., Jaffe A. H., 1999, *Astrophysical Journal*, 515, L1
- Frenk C. S., et al., 2000, arXiv:astro-ph/0007362v1
- Gorski K., 1988, *Astrophysical Journal*, 332, L7
- Gorski K. M., Davis M., Strauss M. A., White S. D. M., Yahil A., 1989, *Astrophysical Journal*, 344, 1
- Hahn O., Angulo R. E., Abel T., 2015, *Monthly Notices of the Royal Astronomical Society*, 454, 3920
- Hockney R. W., Eastwood J. W., 1988, *Computer Simulation Using Particles*. Taylor & Francis, Bristol, PA, USA
- Hubble E., 1934, *Astrophysical Journal*, 79, 8
- Irvine W. M., 1961, Thesis, HARVARD UNIVERSITY
- Jelic-Cizmek G., Lepori F., Adamek J., Durrer R., 2018, *Journal of Cosmology and Astroparticle Physics*
- Jenkins A., et al., 1998, *Astrophysical Journal*, 499, 20
- Jennings E., Baugh C. M., Pascoli S., 2011, *Monthly Notices of the Royal Astronomical Society*, 410, 2081
- Juszkiewicz R., Ferreira P. G., Feldman H. A., Jaffe A. H., Davis M., 2000, *Science*, 287, 109
- Kazantzidis S., Magorrian J., Moore B., 2004, *Astrophysical Journal*, 601, 37
- Klypin A., Prada F., Betancort-Rijo J., Albareti F. D., 2018, *Monthly Notices of the Royal Astronomical Society*, 481, 4588
- Kolmogorov A. N., 1962, *Journal of Fluid Mechanics*, 13, 82
- Kuhlen M., Weiner N., Diemand J., Madau P., Moore B., Potter D., Stadel J., Zemp M., 2010, *Journal of Cosmology and Astroparticle Physics*
- Layzer D., 1963, *Astrophysical Journal*, 138, 174
- Mo H. J., Jing Y. P., Borner G., 1997, *Monthly Notices of the Royal Astronomical Society*, 286, 979
- Peebles P. J. E., 1980, *The Large-Scale Structure of the Universe*. Princeton University Press, Princeton, NJ
- Peebles P. J. E., Melott A. L., Holmes M. R., Jiang L. R., 1989, *Astrophysical Journal*, 345, 108
- Petac M., Ullio P., Valli M., 2018, *Journal of Cosmology and Astroparticle Physics*
- Pueblas S., Scoccimarro R., 2009, *Physical Review D*, 80
- Romano-Díaz E., Van De Weygaert R., 2007, *Monthly Notices of the Royal Astronomical Society*, 382, 2
- Sheth R. K., 1996, *Monthly Notices of the Royal Astronomical Society*, 279, 1310
- Sheth R. K., Mo H. J., Tormen G., 2001a, *Monthly Notices of the Royal Astronomical Society*, 323, 1
- Sheth R. K., Hui L., Diaferio A., Scoccimarro R., 2001b, *Monthly Notices of the Royal Astronomical Society*, 325, 1288
- Springel V., 2005, *Monthly Notices of the Royal Astronomical Society*, 364, 1105
- Taylor G. I., 1935, *Proceedings of the royal society A*, 151, 421
- Taylor G. I., 1938, *Proceedings of the Royal Society of London Series a-Mathematical and Physical Sciences*, 164, 0015
- Ullio P., Kamionkowski M., 2001, *Journal of High Energy Physics*
- Wojtak R., Lokas E. L., Mamon G. A., Gottlober S., Klypin A., Hoffman Y., 2008, *Monthly Notices of the Royal Astronomical Society*, 388, 815
- Xu Z., 2021a, arXiv e-prints, p. arXiv:2109.09985
- Xu Z., 2021b, arXiv e-prints, p. arXiv:2109.12244
- Xu Z., 2021c, arXiv e-prints, p. arXiv:2110.03126
- Xu Z., 2021d, arXiv e-prints, p. arXiv:2110.05784
- Xu Z., 2021e, arXiv e-prints, p. arXiv:2110.09676
- Xu Z., 2021f, arXiv e-prints, p. arXiv:2110.13885
- Xu Z., 2022c, A comparative study of dark matter flow & hydrodynamic turbulence and its applications, doi:10.5281/zenodo.6569901, <http://dx.doi.org/10.5281/zenodo.6569901>
- Xu Z., 2022d, Dark matter flow dataset, doi:10.5281/zenodo.6586212, [https://github.com/ZhijieXu2022/dark\\_matter\\_flow\\_dataset](https://github.com/ZhijieXu2022/dark_matter_flow_dataset)
- Xu Z., 2022a, Dark matter flow dataset Part I: Halo-based statistics from cosmological N-body simulation, doi:10.5281/zenodo.6541230, <http://dx.doi.org/10.5281/zenodo.6541230>
- Xu Z., 2022b, Dark matter flow dataset Part II: Correlation-based statistics from cosmological N-body simulation, doi:10.5281/zenodo.6569898, <http://dx.doi.org/10.5281/zenodo.6569898>
- Xu Z., 2022e, arXiv e-prints, p. arXiv:2202.00910
- Xu Z., 2022f, arXiv e-prints, p. arXiv:2202.02991
- Xu Z., 2022g, arXiv e-prints, p. arXiv:2202.04054
- Xu Z., 2022h, arXiv e-prints, p. arXiv:2202.06515
- Xu Z., 2022i, arXiv e-prints, p. arXiv:2202.07240
- Xu Z., 2022j, arXiv e-prints, p. arXiv:2203.05606
- Xu Z., 2022k, arXiv e-prints, p. arXiv:2203.06899
- Zhao Y., Bi X. J., Yin P. F., Zhang X. M., 2018, *Physical Review D*, 97
- de Karman T., Howarth L., 1938, *Proceedings of the Royal Society of London Series a-Mathematical and Physical Sciences*, 164, 0192